USING AVO ANALYSIS TO DETERMINE THE GAS RESERVOIRS IN THE SOUTH THRACE BASIN, NORTHWEST TURKEY

A Thesis Presented To

The Faculty Of The Department Of Earth And Atmospheric Sciences

University Of Houston

In Partial Fulfillment

Of The Requirements For The Degree

Master Of Science

By

Muhlis Unaldi

December 2012

USING AVO ANALYSIS TO DETERMINE THE GAS RESERVOIRS IN THE SOUTH THRACE BASIN, NORTHWEST TURKEY

_____

MUHLIS UNALDI

APPROVED:

_____

DR. JOHN P. CASTAGNA

_____

DR. EDIP BAYSAL

_____

DR. EVGENI CHESNOKOV

_____

Dean of College of Natural Sciences and Mathematics

DEDICATION

This research is dedicated to my lovely sister, Funda Unaldi Nalbantoglu, for the constant love, patience, encouragement, and prayers, particularly during my Master's education.

ACKNOWLEDGEMENTS

I would like to express my greatest appreciation and gratitude to my family and friends.

I would like to extend my gratitude to Dr. Edip Baysal and Dr. Evgeni Chenokov for all their guidance and support. Dr Edip Baysal taught me a lot, and he was always there whenever I needed his advice.

My adviser, Dr. John Castagna, taught me a lot about science. I enjoyed every single conversation with him, including in or out of the classroom. He is an exceptional scientist.

At the end, I'd like to thank Turkish Petroleum Corporation for this great learning opportunity to pursue a MS degree in Geophysics.

USING AVO ANALYSIS TO DETERMINE THE GAS RESERVOIRS IN THE SOUTH THRACE BASIN, NORTHWEST TURKEY

An Abstract of a Thesis Presented to

the Faculty of the Department of Earth and Atmospheric Sciences

University of Houston

In Partial Fulfillment

of the Requirements for the Degree

Master of Science

By

Muhlis Unaldi

December 2012

ABSTRACT

This study investigates gas reservoirs using AVO modeling and analysis for 3D pre-stack seismic data acquired by Turkish Petroleum Corporation in the Thrace Basin located in the northwest part of Turkey. The Thrace Basin is Turkey's the most productive onshore gas province, and is the largest and thickest sedimentary basin in Turkey. The Thrace basin is basically a vertical stack of sand-shale-silt sequences with no complex structures or salt domes. In such sedimentary stacks, rock properties such as density and velocity to calculate Poisson's Ratio and preserving amplitude are very significant in order to obtain a successful AVO result. These features can help determining reservoir locations and increasing gas productivity.

The main objective of this thesis is to understand rock properties at the possible reservoir zone, to do AVO (Amplitude Versus Offset) modeling, and to test the effectiveness of AVO modeling and analysis on the pre-stack seismic reflection data acquired over the Thrace Basin to identify new reservoirs.

In this study, several processing steps were applied to our data, including true amplitude recovery, normal move out correction, pre-stack time migration, correlation of log and seismic data, and well log interpretation. Synthetic data were generated and elastic parameters obtained on synthetic and real data. Conventional AVO analysis techniques were applied; however, the effects of the hydrocarbon saturation to the amplitude could not be highlighted in the reservoir zone. Therefore, three different inversion techniques were performed to obtain an accurate reservoir signature. The inversion techniques could

help to map the reservoir zone in a better way by increasing the vertical resolution.

CONTENTS

LIST OF FIGURES

LIST OF TABLES

Introduction

A robust combination of AVO analysis techniques and the latest software packages yields top-notch improvements to identify new reservoirs.

This study takes place in one of the most important hydrocarbon provinces of Turkey. The Thrace Basin is Turkey's the most productive onshore gas province, and is the largest and thickest sedimentary basin in Turkey. There are three major units, the Danisment Formation, Osmancik Formation, and Mezardere Formation, which produce gas in the basin. In the early Oligocene sequence, sandstones and carbonates show good signals in terms of reservoir properties. Stratigraphic and structural traps exist in the Thrace Basin, and play a very significant role in gas and oil exploration. Gas has been discovered in the Osmancik, Mezardere, Hamitabat, and Sogucak Formations. The reservoir rock sandstones in the Osmancik, Mezardere, and Hamitabat Formations contain clayey sandstones and sandy limestones.

The main objective of the thesis is to understand rock properties at the possible reservoir zone, to do AVO (Amplitude Versus Offset) modeling, and to test the effectiveness of AVO modeling and analysis on the pre-stack seismic reflection data acquired over the Thrace Basin to identify new reservoirs.

We used conventional velocity and amplitude analysis, and we also tried to relate the hydrocarbon saturation to the amplitude or velocity variation. We could not highlight the reservoir zone in AVO volume attribute sections; therefore, we performed three different inversion techniques to increase the vertical resolution and to obtain an

accurate reservoir signature. This could help us to better find the next drilling zone.

Chapter 1: Geologic Background

1.1 Geological Setting

Turkey has seven basins onshore; the Anatolia Basin, Thrace Basin, Adana Basin, Tuz- Golu Basin, East Anatolia Basin, Black Sea Basin, and Sinop Basin. Moreover, there are four major basins offshore; the Black Sea Basin, Marmara Sea Basin, Aegean Basin, and Mediterranean Sea Basin.

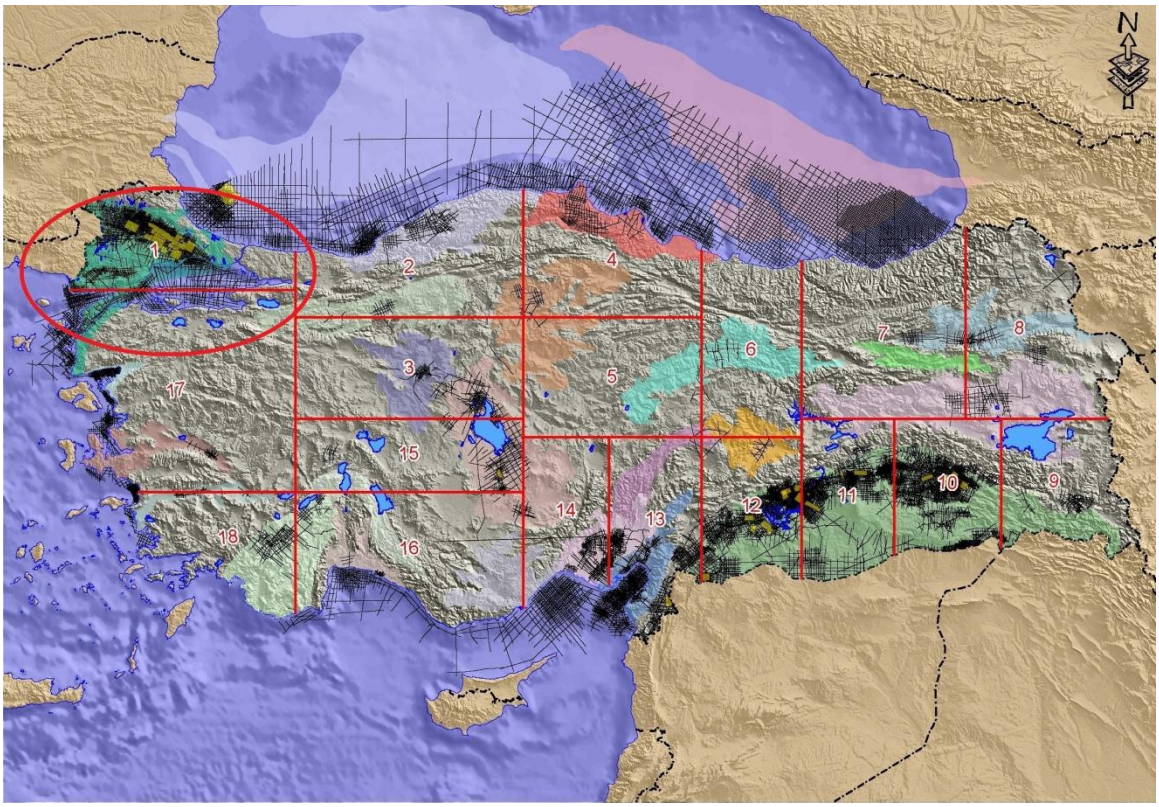

Figure 1.1 Thrace Basin with deployed seismic profiles.

The Thrace Basin, is a triangular shaped Tertiary basin, filled with approximately 9000 m sedimentary rocks, cumulative thickness was estimated (Turgut *et al.*, 1991). The basin is in the European part of Turkey; it has borders with Greece and Bulgaria

(Figure 1.1). The basin is surrounded with the Rhodope Massif on its west, the crystalline Strandja Mountain Belt and western end of the Black Sea on its north, and Marmara Sea on its south (Figure 1.2).

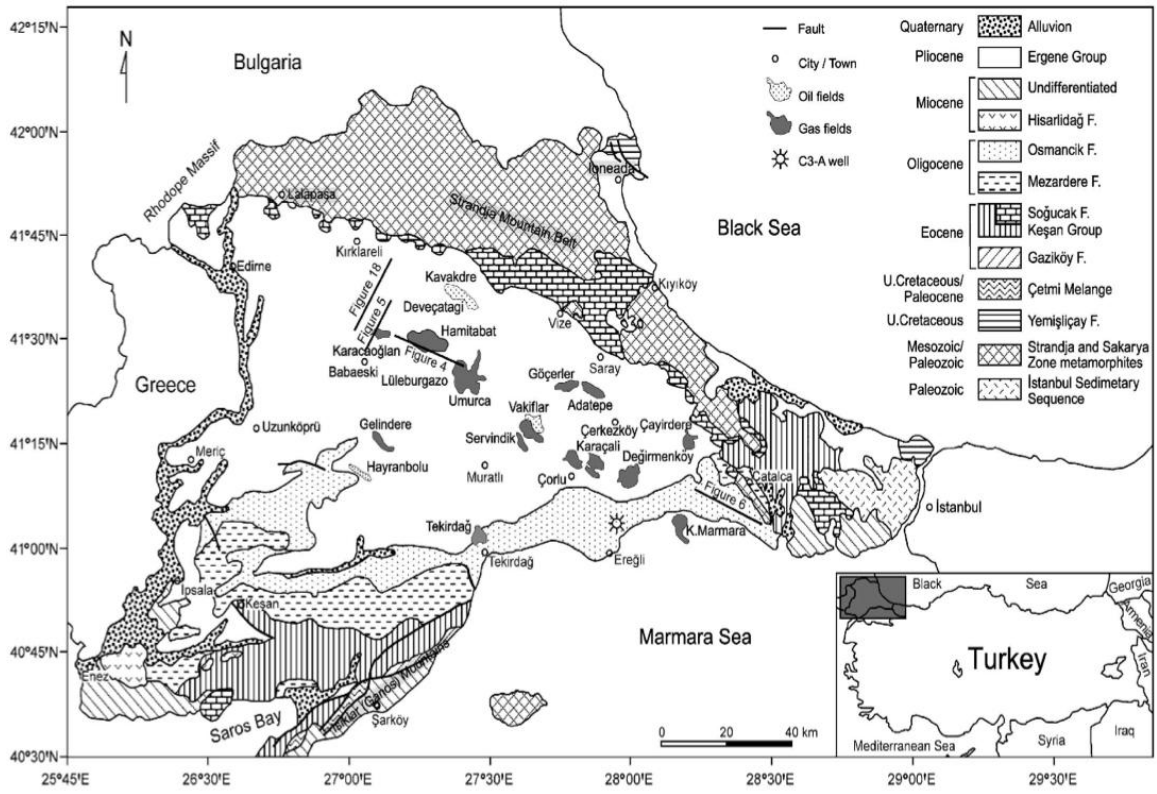

Figure 1.2 Location and geological map of the Thrace Basin showing gas and oil fields (modified from Turgut et al., 1991).

Deposition first started with an extension of the Pontid Plate that was under the intense effects of compressional tectonism in the early Eocene. The southwest-northeast marine transgression was caused by the early extension of the Pontid Plate. Deposition of the thick interbedded sandstone, conglomerate, and shale sequences began in the Eocene and continued until the end of early Miocene. These depositions are more than 8000m (26200 ft) thick (Huvaz *et al*., 2005). The central part of the

basin became overpressured in the late Miocene, and due to this abnormal pressure the south part, was uplifted and tilted towards north. As a result, several low angle thrusts were created. These thrusts have been causing gravity sliding.

The Trace Basin consists of two main groups; the pre-Tertiary crystalline rocks of the basement and overlying the Tertiary sedimentary rocks. The Tertiary rocks include interbedded clastics, lava flows, and tuffaceous deposits. The Tertiary unit is stratigraphically divided into three groups; the Kesan Group, Yenimuacir Group, and Ergene Group. The Danisment, Osmancik, and Mezardere Formations contain reservoir rocks, and they belong to the Yenimuacir Group. These formations are buried more than 3000 m deep, and are exposed to temperatures 80-140 °C (Figure 1.4). Our seismic section and wells go through these formations.

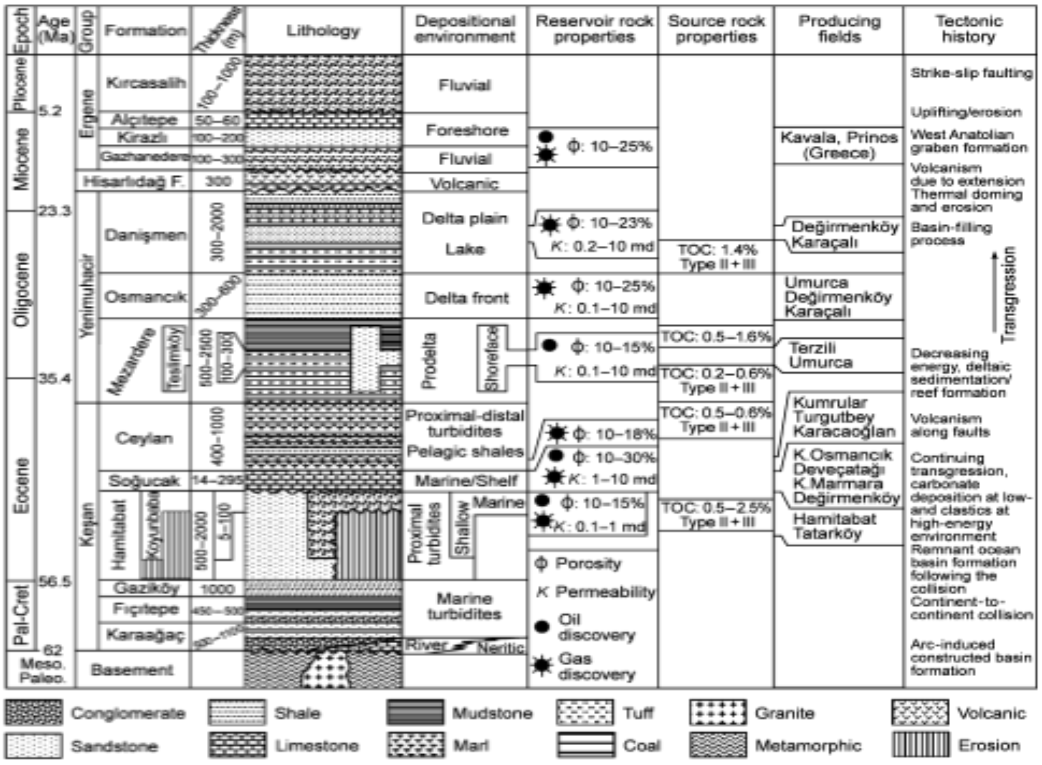

Figure 1.3 Generalized stratigraphy of the Thrace Basin showing the depositional environments, formation thicknesses, petrophysical properties of the reservoir rocks, type and average percent of total organic carbon (TOC) of the source rocks and producing fields (modified from Huvaz *et al*., 2005).

1.2 Petroleum System of Thrace Basin

This study takes place in one of the most important hydrocarbon provinces of Turkey. In the early Oligocene sequence, sandstones and carbonates show good signals in terms of reservoir properties (Figure 1.2). Stratigraphic and structural traps exist in the Thrace Basin, and play a very significant role in gas and oil exploration. Gas has been discovered in the Osmancik, Mezardere, Hamitabat, and Sogucak Formations. The reservoir sandstones in the Osmancik, Mezardere, and Hamitabat Formations contain clayey sandstones and sandy limestones. The Sogucak Formation contains oil

which has been discovered by Turkish Petroleum Corporation (TPAO). The porosity of the sandstones in the reservoirs, which are in the Danisment and Osmancik Formations, range from 10 to 25%. On the other hand, the Mezardere and Hamitabat Formations gas fields porosity ranges from 5 to 15%. Our reservoir is located in the Oligocene-aged Osmancik and Mezardere Formations. Three reservoir source rocks from the upper Hamitabat Formation, Ceylan Formation, and lower Mezardere Formation, with valuable organic content, were observed in the Thrace Basin. Other formations also contain organic carbon; however, they do not have enough carbon to become an active source of rock.

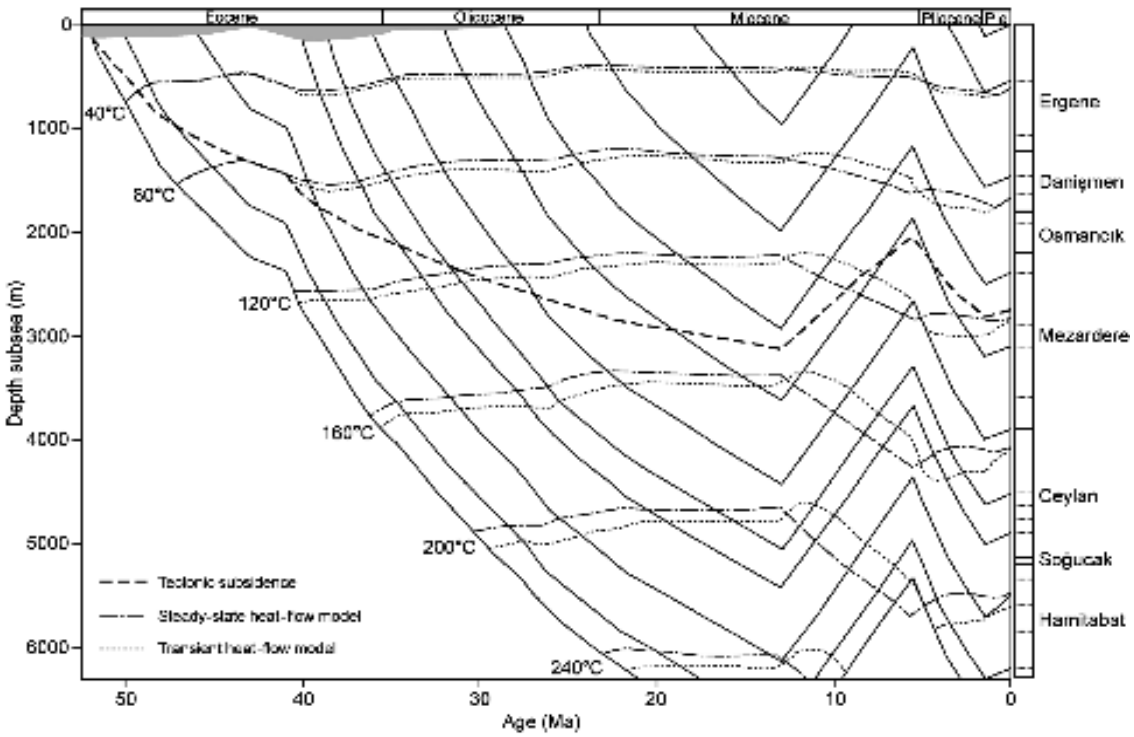

Figure 1.4 Burial history and the isotherms constructed using steady-state (dashed dot-dash line) and transient (dotted line) heat-flow models (from Huvaz et al., 2005).

Chapter 2: Data Set

The Umurca Field in the Thrace Basin dataset came from TPAO in order to analyze it for my thesis study. The 3D data were gathered from east-west located receivers with the angle of 27.28° (-62° at Crossline direction +90°). Moreover, the receiver arrays were located apart 25m. The Vibrator points were spaced 50m apart. Four inline Vibro-seismic trucks were used as sources.

The acquisition, bin sized 25m by 25 m, was created by 25m receiver spacings and 50m source spacings. The 3D data contain 27.3° east-west oriented 564 inlines and -62.7 ° north-south oriented 625 crosslines (Figure 2.1).

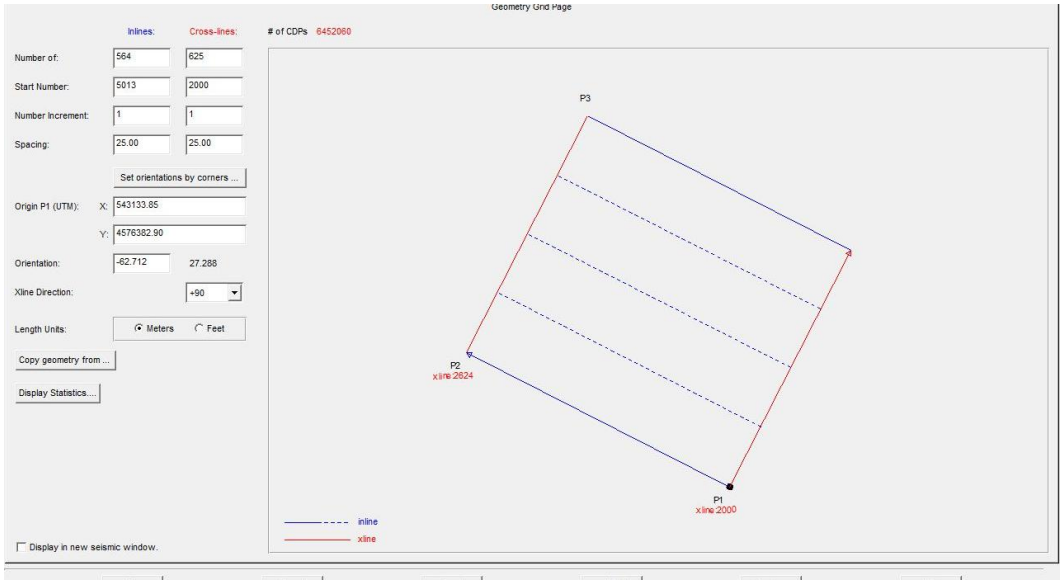

Figure 2.1 Inline and crossline orientation and spacing from HR screenshot.

We have 3 wells (Well A, Well B, and Well C) in the area with various logs as explained with units and symbols in table 2.1. Well x and y locations, surface

elevations, corresponding inlines, crosslines, and CDP numbers are indicated in (Figure 2.2).

Table 2.1 Different types of logs that were included in the dataset with their acronym and unit of measure.

ACRONYM	UNITS	TYPE OF WELL
GR	API	Gamma Ray
SP	mV	Self Potential
DT	μs/ft	Sonic Velocity
RHOB	g/cc	Bulk Density
LLD	Ohm-m	Deep Lateral Log
LLS	Ohm-m	Medium Lateral Log
Cal	Inc	Caliper
NPHI	%	Neutron Porosity
DRHO	g/cc	Density Correction
CS	ms	Check Shots

Well Name	Units	X Location	Y Location	Inline	Xline	CDP
Well_A	m	535277.59	4585812.21	5204	2452	119828
Well_B	m	536777.06	4585170.69	5209	2387	122888
Well_C	m	536673.47	4585290.69	5211	2393	124144

Figure 2.2 Well locations.

In this study, the Well C was chosen to be used in order to process the data, because it has the deepest and the highest number of the logs among the wells. The reservoir thickness was determined by using GR, DT, and RHOB logs.

Chapter 3: Data Enhancement

The first process started by loading gathers into the Hampson-Russell Software for analysis and further processing. The key point to load the data correctly is matching inline and crossline byte locations parameters with the right corresponding values from the header (Figure 3.1). The Thrace Basin dataset was sent from TPAO as true amplitude recovery process applied and NMO-corrected 3D gathers (Figure 3.2). We decided to apply the Radon Noise Suppression and Trim Static steps to remove the random noise and flatten the layers caused by over/under NMO corrections.

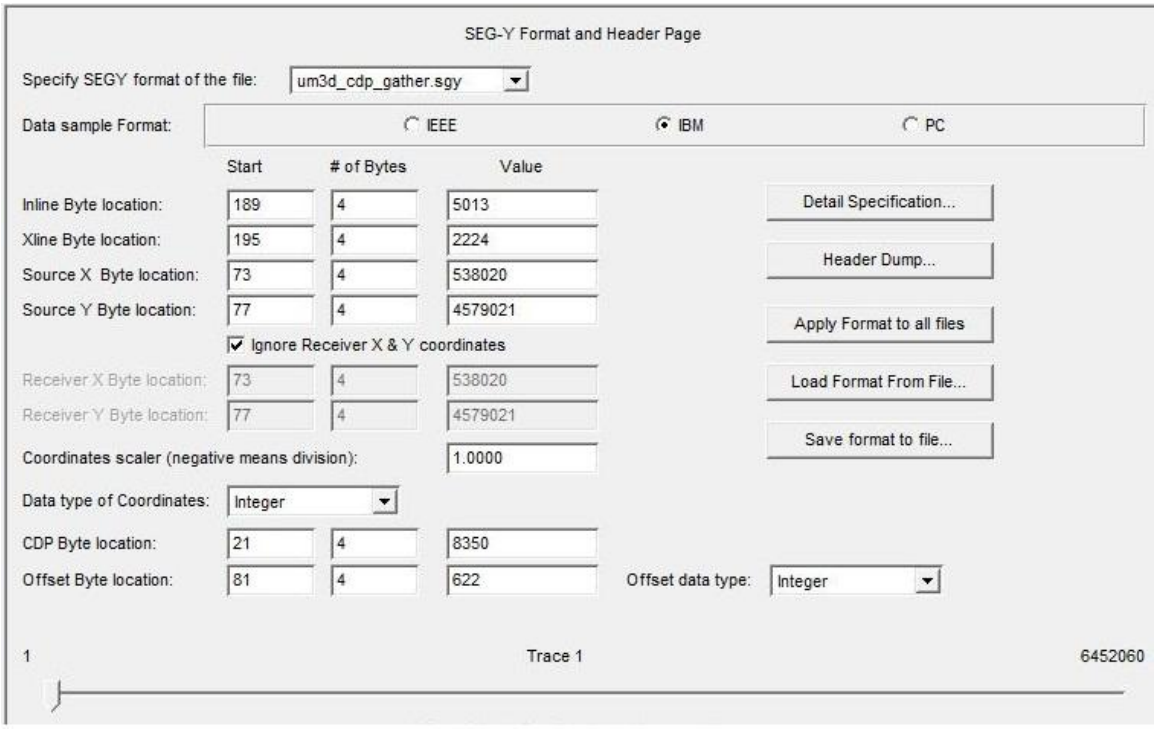

Figure 3.1. Inline and crossline parameters from header.

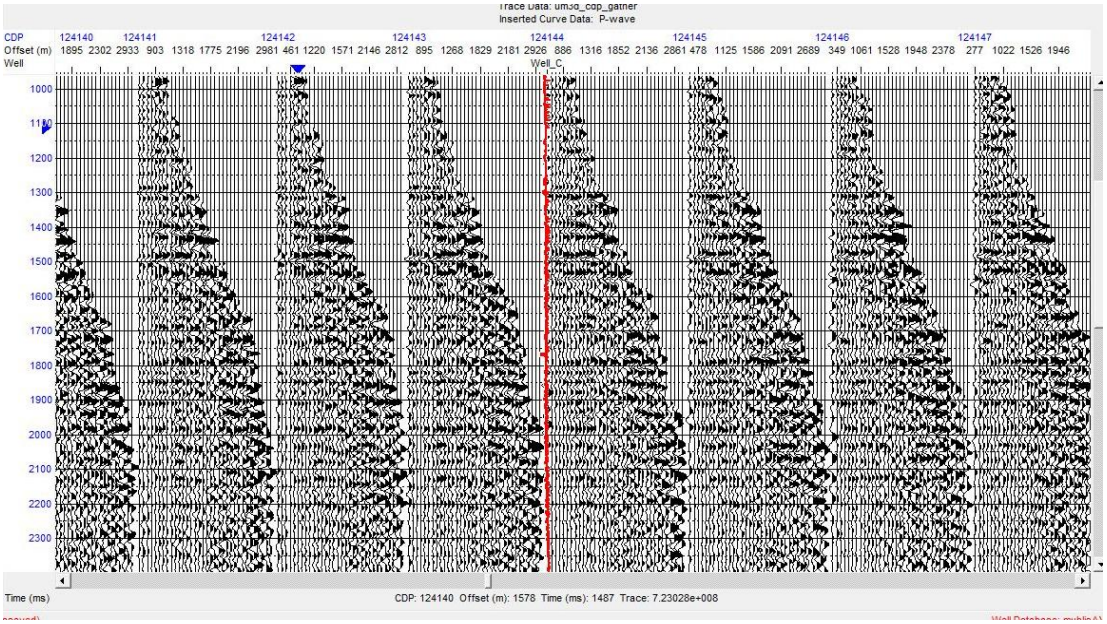

Figure 3.2 True amplitude recovery process applied and NMO-corrected gathers.

3.1 Radon Noise Suppression and Trim Static Application

After loading gathers into the Hampson-Russell software, we used the "Invest" tool to remove the random noise from the data. The Invest tool has two options; the Multiple Suppression and the Radon Noise Suppression. However, we only used the Radon Noise Suppression tool to remove the random noise. We applied the radon process several times by changing the parameters to remove the noise, by preserving the real data, and decided the optimum radon parameters as shown in Figure 3.3. After the radon process, the data were cleaned up from the random noise, but we were still able to recognize the effects of miss-NMO correction at far offsets (Figure 3.4).

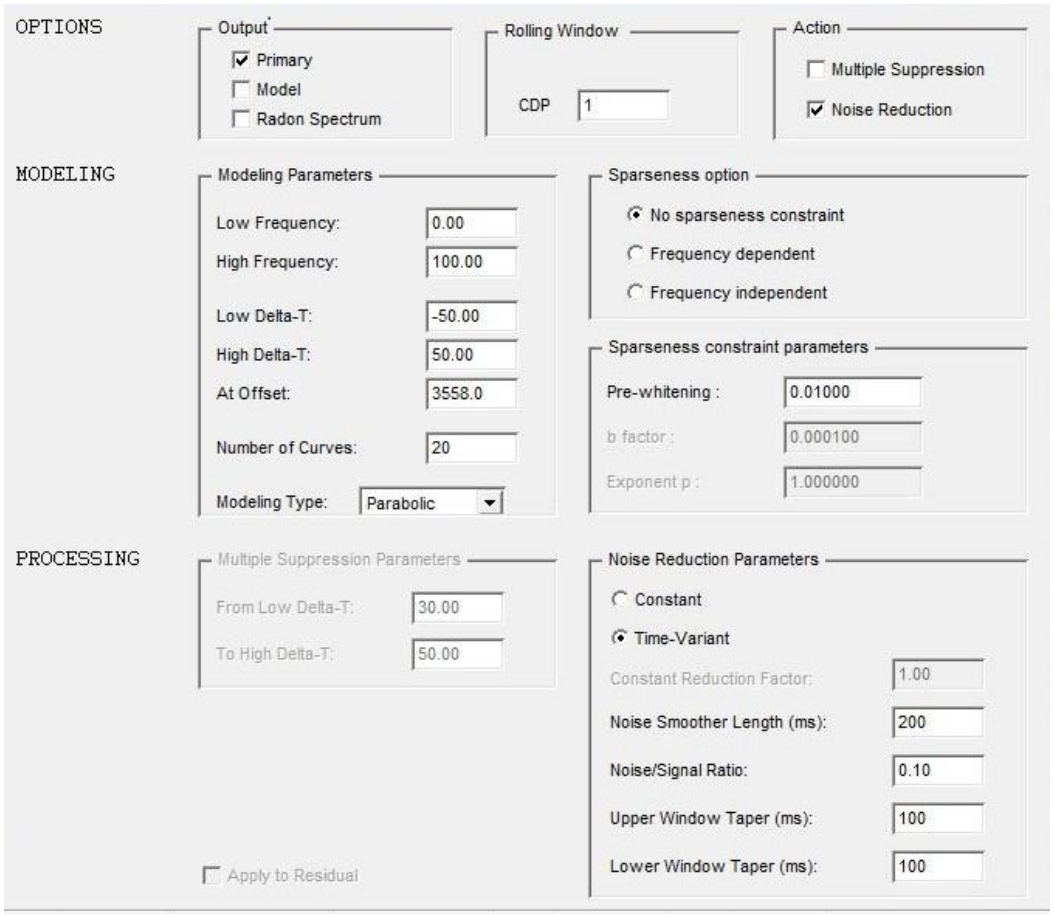

Figure 3.3 Radon parameters.

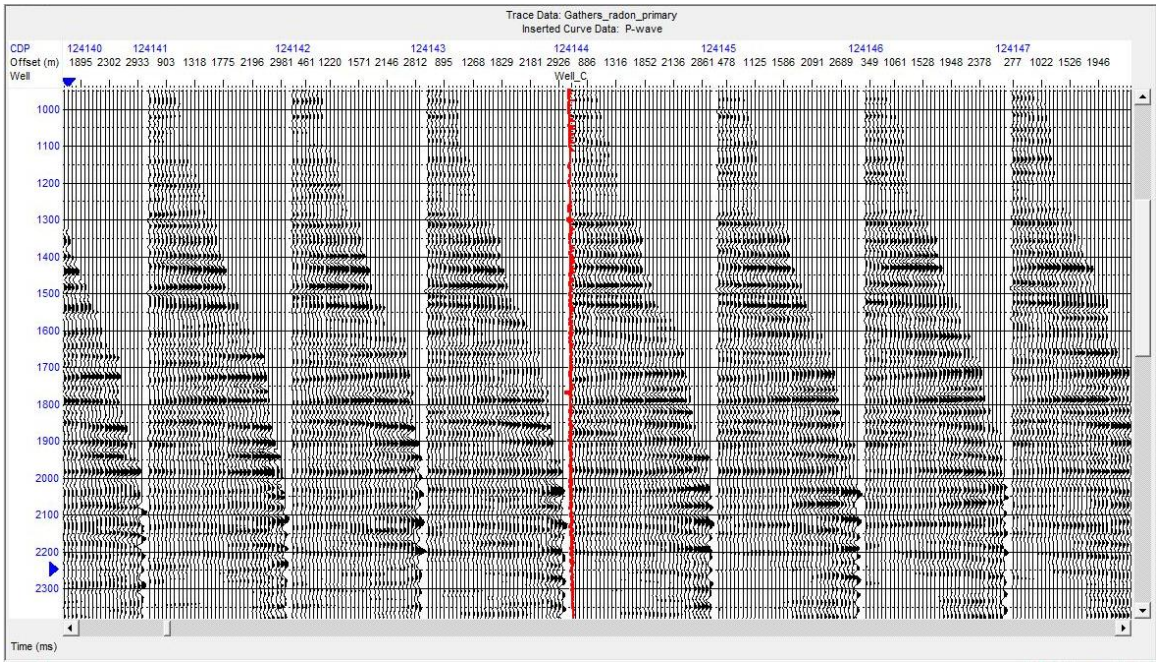

Figure 3.4 Radon noise suppression applied offset gathers.

The Trim Static process was applied to the data, which were previously cleaned of random noise by applying the Radon Noise Suppression, to get rid of the remaining effects of the NMO correction. In the Trim Static process, we defined a 20ms time window to align and to shift the traces in that interval for the each trace in the gather. After Trim Static process, we observed the enhancements at near offsets, but we were not able to completely remove the effects at the far offsets (Figure 3.5).

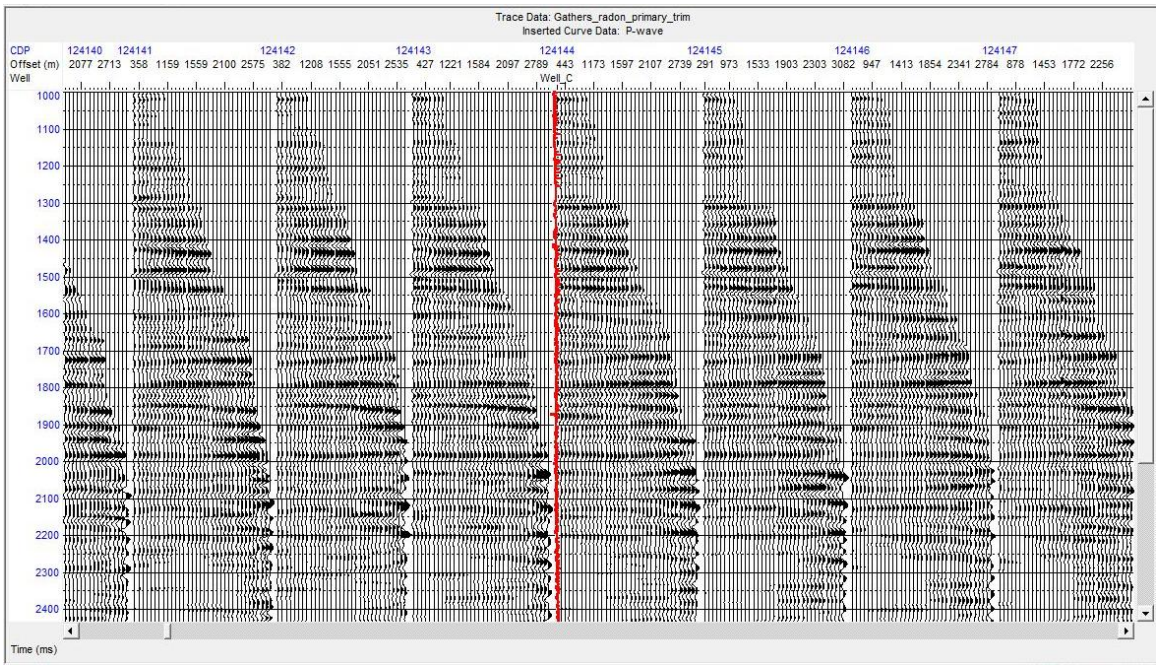

Figure 3.5 Offset gathers after trim static and radon noise suppression.

3.2 Creating Super Gathers, Angle Gathers, and CDP Stacks

3.2.1 Super Gather

We created a super gather using the shifted CDP gathers. Creating a super gather enhances the signal to noise ratio and helps to eliminate the random noise. The super gather was created by averaging over 5 CDP bin locations. In the each output bin, we have 10 offsets ranging from 14 to 3558 meters. We observed that the signal to noise ratio at the interest zone at 1400 ms was improved (Figure 3.6).

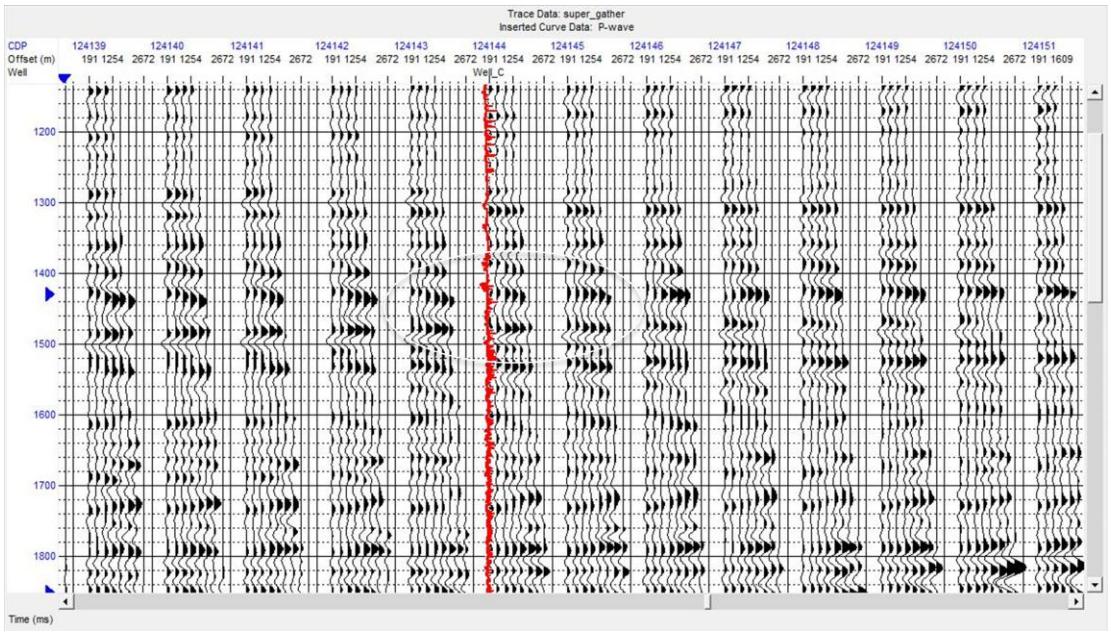

Figure 3.6 Super gather with marked reservoir zone.

3.2.2 Angle Gather

We must determine the range of the angle of incidence at the interest zone to do AVO analysis correctly. For that reason, we displayed the incident angle in colors on the super gather display to decide it (Figure 3.7).

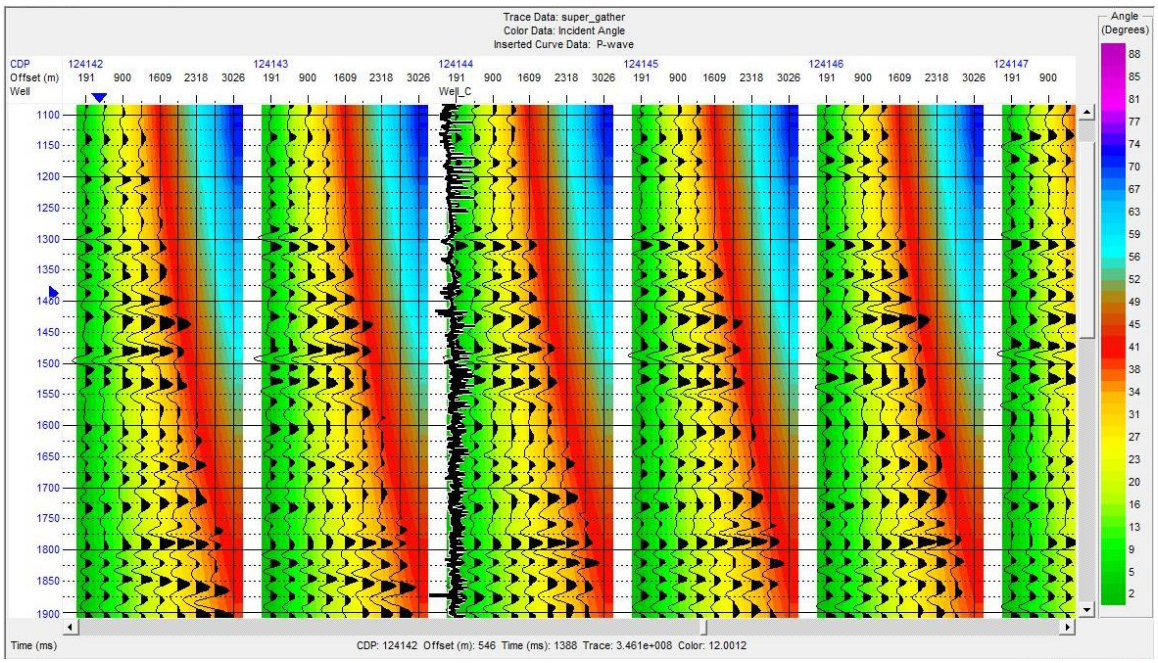

Figure 3.7 The incident angle color display on super gather.

The maximum angle at the interest zone is around 36 degrees in the incident angle color display. We have to use a specific velocity field to create an angle gather. In our study, we used the sonic log as the velocity field to convert offsets to angles. We can state that the ranges of angles change depending on the velocity input. In the angle gather display, the angles are ended at 36 degrees (Figure 3.8). The created angle gather volume will be used in the later processes such as the Simultaneous Inversion.

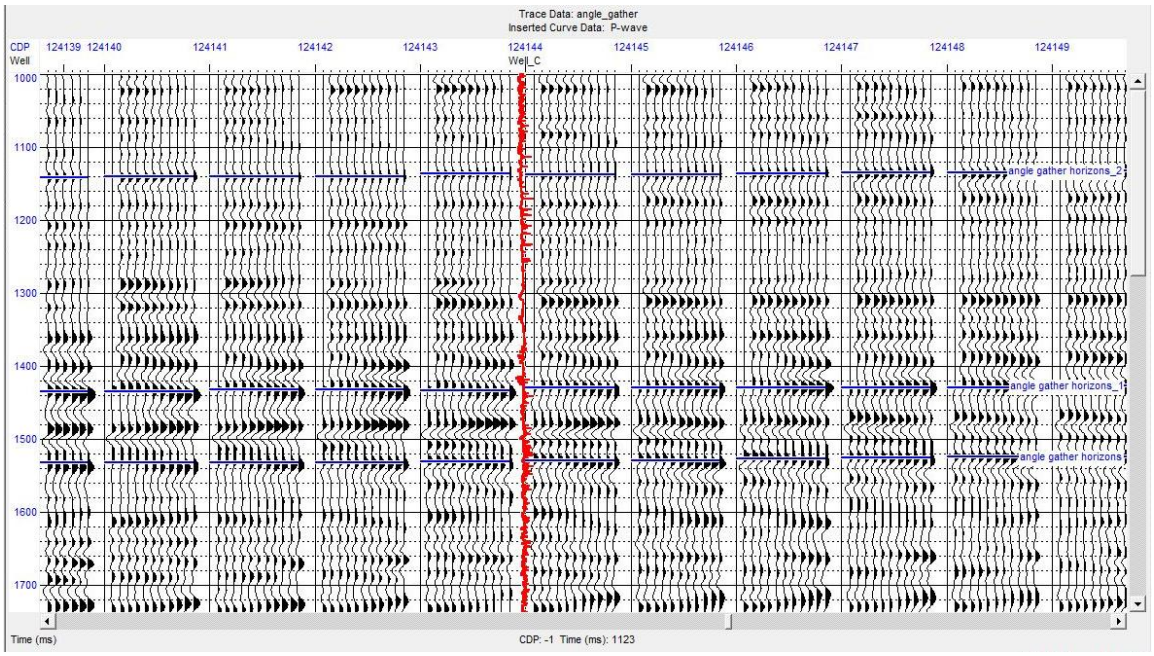

Figure 3.8 Angle gather.

3.2.3 CDP Stack

We created a CDP stack by using 15000 CDP gathers time interval from 1000 to 3000 ms and the offset spanning range from 14 to 3558 meters by one bin. We observed the anomaly at the zone of interest (Figure 3.10). The CDP stack volume also will be used in the later processes.

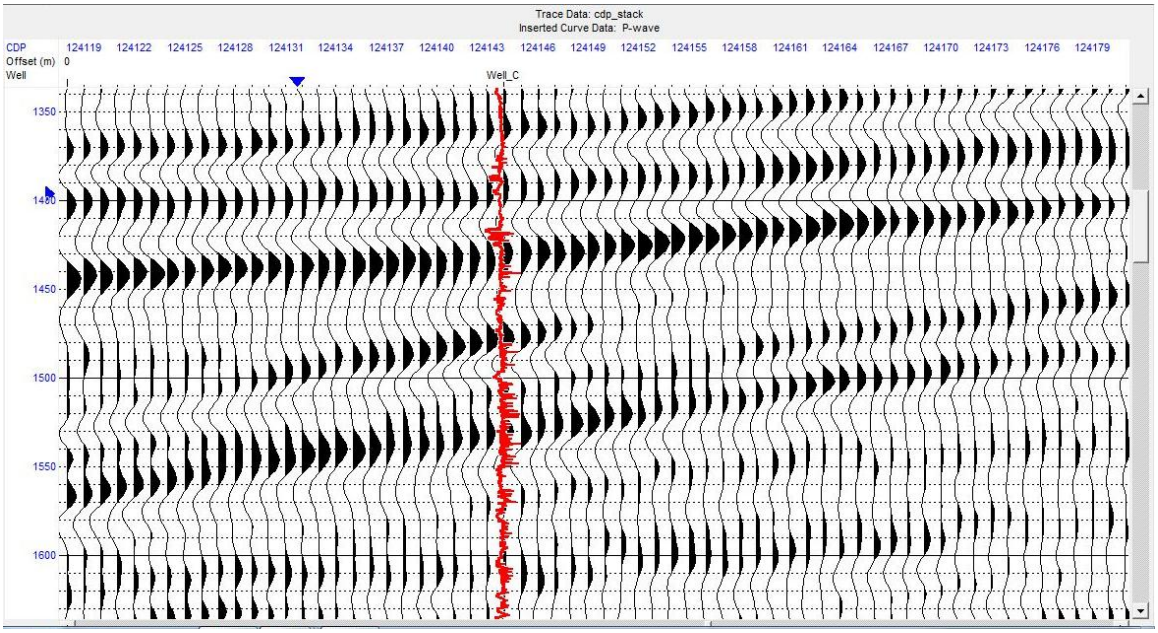

Figure 3.9 CDP stack zoomed in the zone of interest.

Chapter 4: AVO Analysis and Inversion Techniques

We are ready to start the well-log editing process and then proceed to the AVO analysis after data enhancement, producing the CDP gathers, and generating the post-stack seismic sections. For such analysis, we have been using the Hampson-Russell software.

4.1. AVO Analysis

Seismic properties of the media result the wave propagation and eventual signature when the wave propagates through the media. Seismic properties are P- and S-wave velocities, bulk density, bulk modulus, shear modulus, and Lame's parameters. The sediments, extent of compaction, and burial history control this situation. The geologic framework plays the key role to have successful AVO results, and it requires good understanding.

In AVO analysis, we evaluate the reflectivity as a function of offset. The method widely used to validate gas-sand-based seismic amplitude anomalies (Ostrander, 1984). Any bright spots in the seismic sections do not mean that they were caused by gas-sands. Around 1970s, people drilled every bright spot in the seismic section, but some of them were unsuccessful. Interpreters sometimes refrain to use the method due to the pitfalls. For example, shales may have higher impedance than gas-sands, and their reflections' coefficients may increase with offset. The AVO analysis is a robust tool to eliminate pitfalls. This method requires very meticulous process steps so as to be done to distinguish these properties properly and to have the correct AVO

characteristics.

The Zoeppritz Equations can be called first AVO equations. The change in elastic rock properties across the interface and the angle of incidence cause variations in offset depended reflection amplitudes. The general approach for the Zoeppritz Equations is to explain variation of these amplitudes with offset depending on physical properties of the rocks in the interest zone. The Zoeppritz Equations were simplified by the Aki-Richard Approximation in order to serve better for practical purposes. This is written in three terms; P-wave, S-wave, and density. When zero offset reflectivity is <<1, the Zoeppritz Equations and Aki-Richard's Approximation give very similar results (Li *et al*., 2007).

The Shuey's Approximation is used very commonly to explain AVO anomalies. According to the Shuey's Equation, reflections occur at the boundary with an incident angle θ. The Shuey's Equation's first-order approximation is:

$$R(\theta) = R_0 + B\sin^2(\theta) \tag{4.1}$$

where $R(\theta)$ is the reflection coefficient at an incident angle θ, R_0 is the zero offset reflection coefficient, and B is the gradient (slope) which produces the AVO response.

4.1.1 AVO Reservoir Sand Classification Scheme

Gas-sands were grouped into four classes considering their shale / sand reflectivity based on the Zoeppritz (1919) Equations. Each class is defined by its normal

incidence reflection coefficient. Several factors such as bed tunning, attenuation, and propagation effects are discarded. Four classes are summarized as follows:

Class 1: High Impedance Sands

The sands impedance is higher than the surrounding shales. This class is referred to "Dim Spot" at near offsets and "Phase or Polarity Reversals" at large offsets. At the shale/ sand interface, a large positive value for the zero offset reflection coefficient is observed at the shale/ sand interface. Sands must be mature and compact to get this effect.

Class 2: Near-zero Impedance Sands

The impedance is quite small and very small positive reflection coefficients are at the top of the reservoir, then it converts to negative value at far offsets. Noise affects negatively detection of this class. This type is referred as "Phase or Polarity Reversals".

Class 3: Low Impedance Sands with Increasing AVO

Negative reflection at the top of the reservoir is observed. The amplitudes get more negative with increasing angles of incidence. This type is referred as "Bright Spots". In this situation, polarity change does not occur.

Class 4: Low Impedance Sands with Decreasing AVO

This class is similar to Class 3, but the amplitudes get slightly less negative with increasing angles of incidence than Class 3.

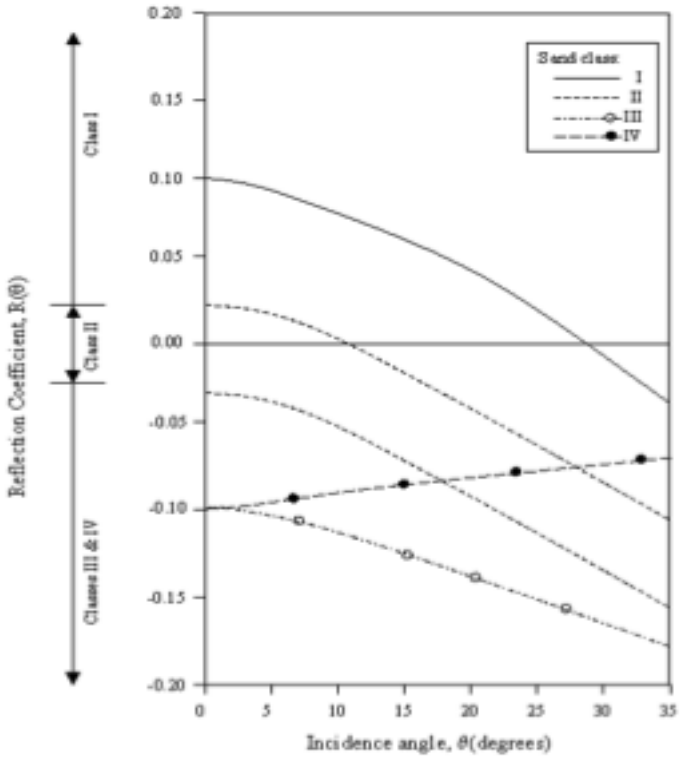

Figure 4.1 Classification of gas-sand (Castagna *et al*., 1998).

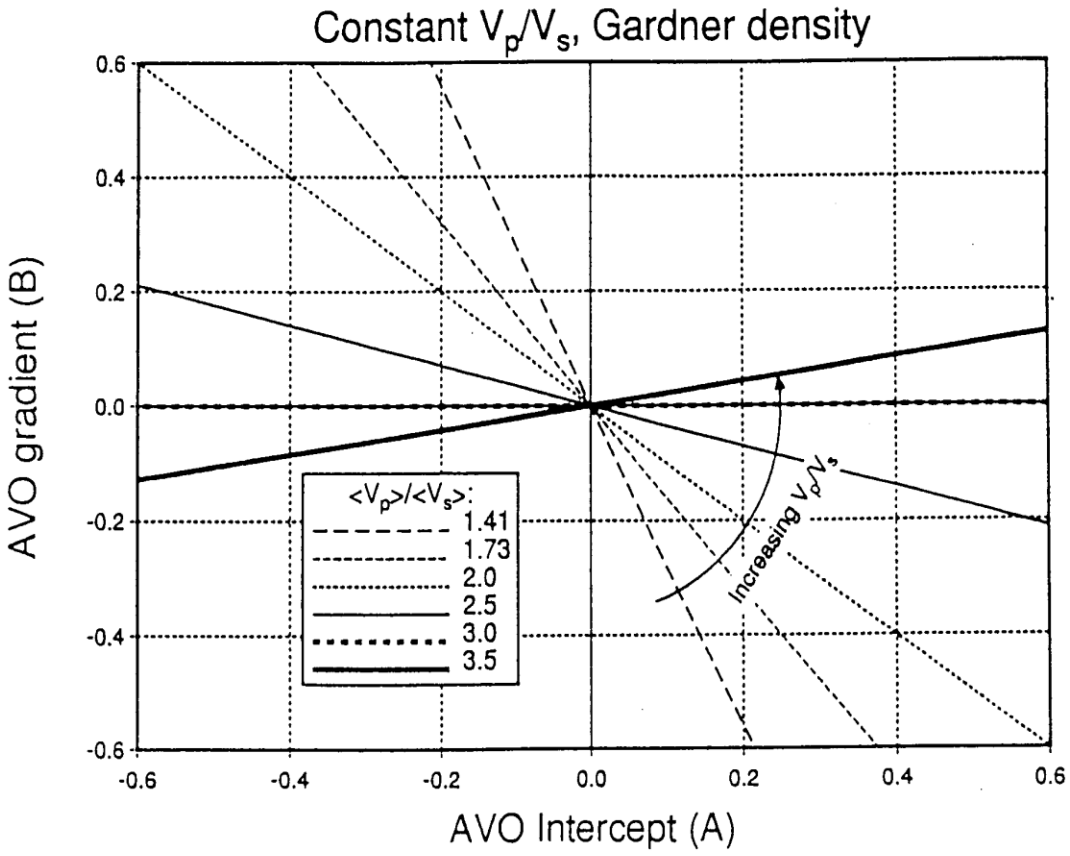

Figure 4.2 AVO intercept A versus gradient B crossplot showing four quadrants (Castagna *et al.*, 1998).

4.2 Inversion Techniques

In this section, inversion techniques can be divided into two groups; pre-stack inversion and post-stack inversion. In this study we only deal with three AVO inversion techniques; the Elastic Impedance Inversion, Lamda-Mu-Rho Inversion, and Simultaneous Inversion.

4.3 AVO Analysis and Inversion Techniques Application

4.3.1 Seismic-Well Tie Process

After enhancing the data, wells loaded into the software using “Elog” tool. The first step is to apply the check shot correction to the sonic log. We statistically extracted several wavelets using the modeling tool in order to perform high correlation between the seismic and the well logs. A wavelet, extracted from the time frame 1000 to 2000ms and the offset range 0 to 2500m with a 200ms wavelength, which was used to have a high correlation coefficient (Figure 4.3). After stretching and shifting the data 76ms, we achieved a 0.94 correlation coefficient (Figure 4.4).

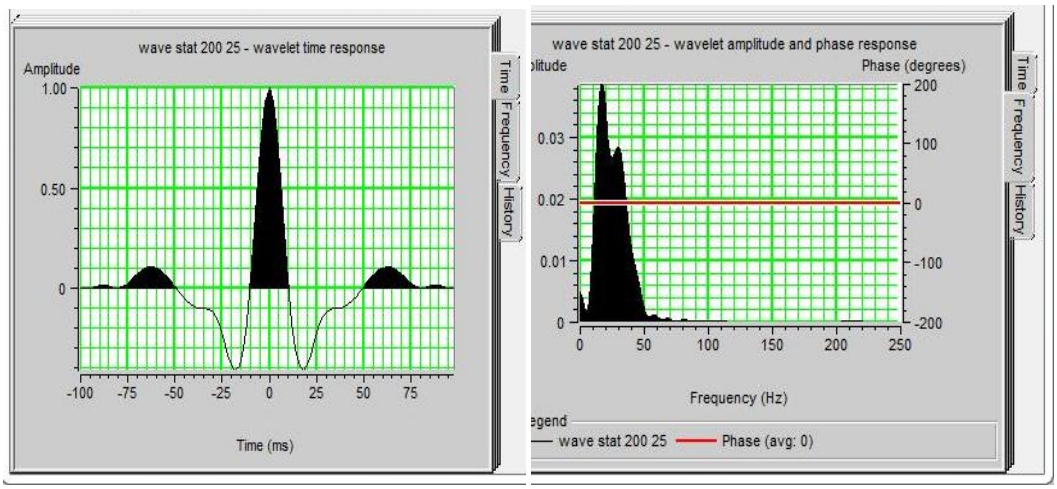

Figure 4.3 The wavelet in the time domain (left) and in frequency domain (right).

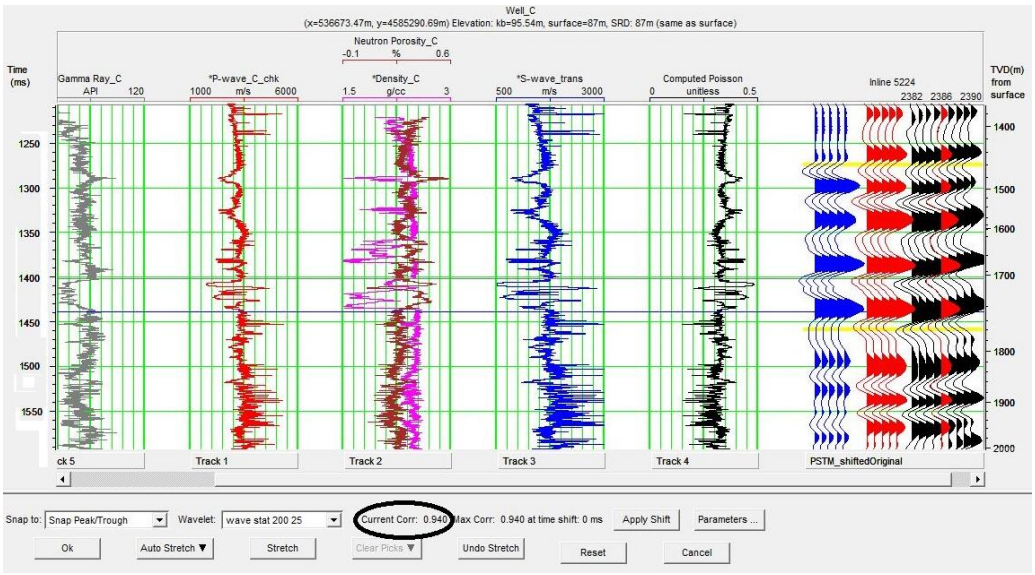

Figure 4.4 Seismic-well tie with correlation coefficient 0.94.

4.3.2 AVO Analysis Application

After the seismic data were processed and enhanced, we were ready to use the CDP gathers as an input of the AVO analysis. The gathers loaded into the software considering inline/crossline locations carefully. Here are the steps that we followed in this AVO process:

1. Loaded logs and determined possible reservoir zone at 1400ms.

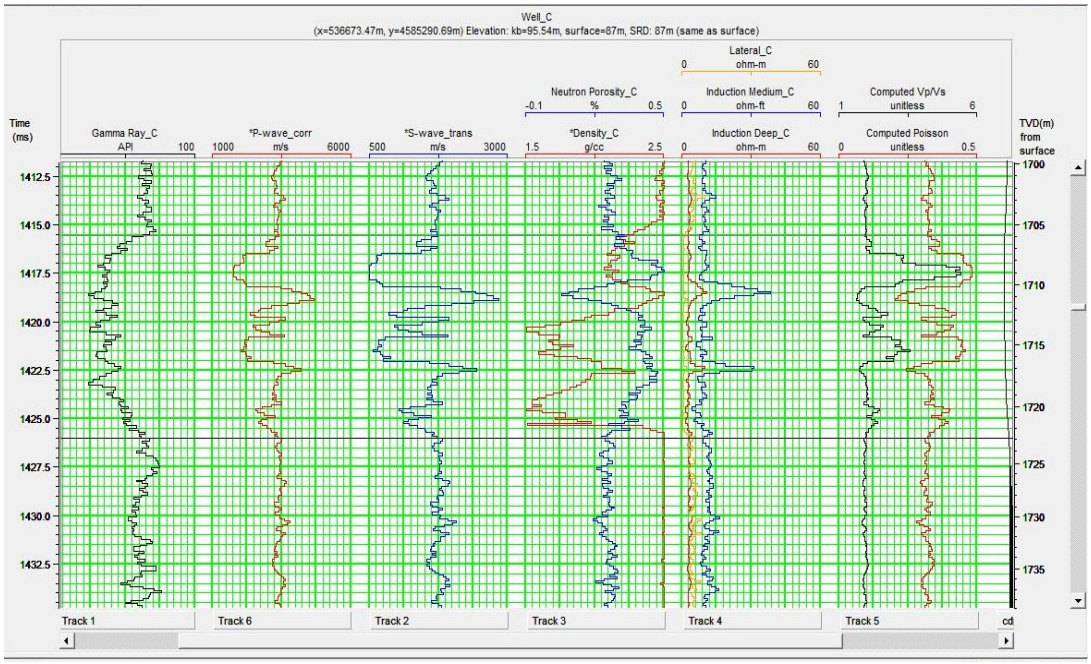

Figure 4.5 Marked possible reservoir zone.

2. Started with a single AVO model. We used Well C and continued modeling for this well.
3. Created a super gather using the shifted CDP gathers by averaging over 5 CDP bin locations. Creating super gathers enhance the signal to noise ratio and helps to eliminate the random noise. The CDP stack was also created to use on the post-stack analysis.
4. Extracted a wavelet from the time frame 1000 to 2000ms and the offset range 0 to 2500m with a 200ms wavelength also achieved a very high 0.94 correlation coefficient. We generated synthetic gathers using the Zoepritz, Aki-Richard's, and Elastic Wave techniques.

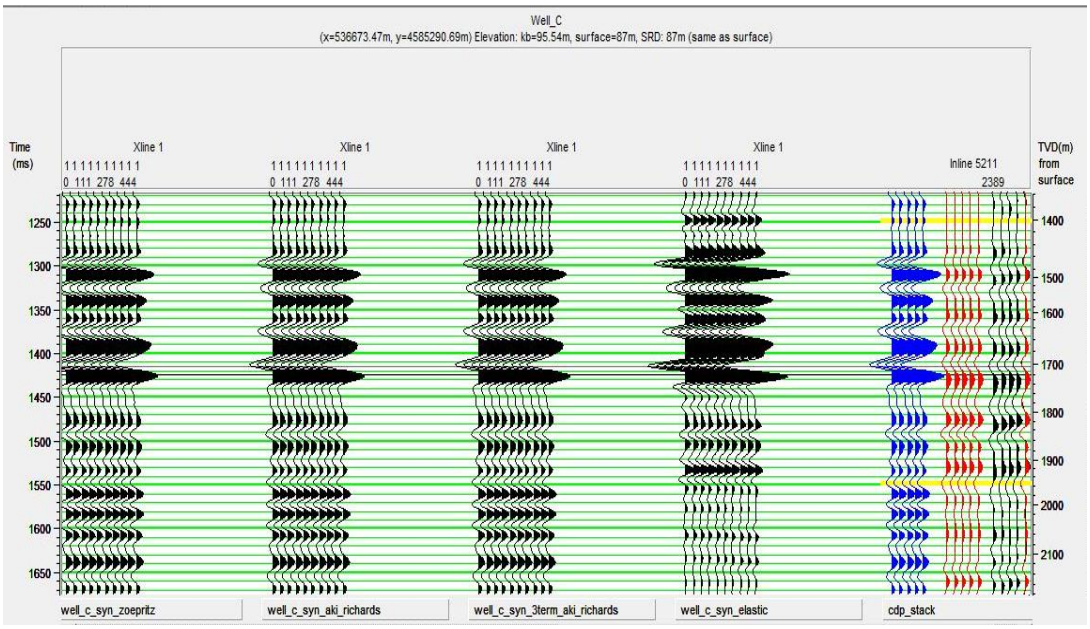

Figure 4.6 Synthetic gathers generated using the Zoepritz, Aki-Richard's, and Elastic Wave techniques.

5. Determined the incident angle using super gathers after a successful seismic-well tie process. The zone of interest's maximum angle of incidence is 36 degrees. The angle gather is also created to be used in the elastic inversion process.
6. Started the AVO analysis with the AVO Volume tool. The horizons were picked involving the zone of interest.

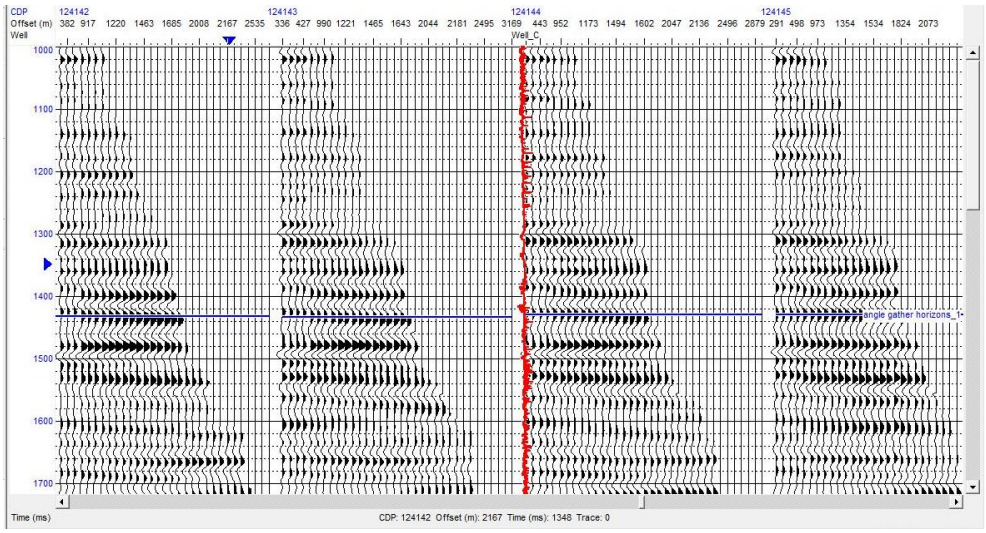

Figure 4.7 Picked horizons on CDP gathers.

7. Calculated gradient A and intercept B. We plotted the AVO attribute volume based on the intercept, gradient, and scaled Poisson's Ratio values to identify the zone of interest for crossploting.

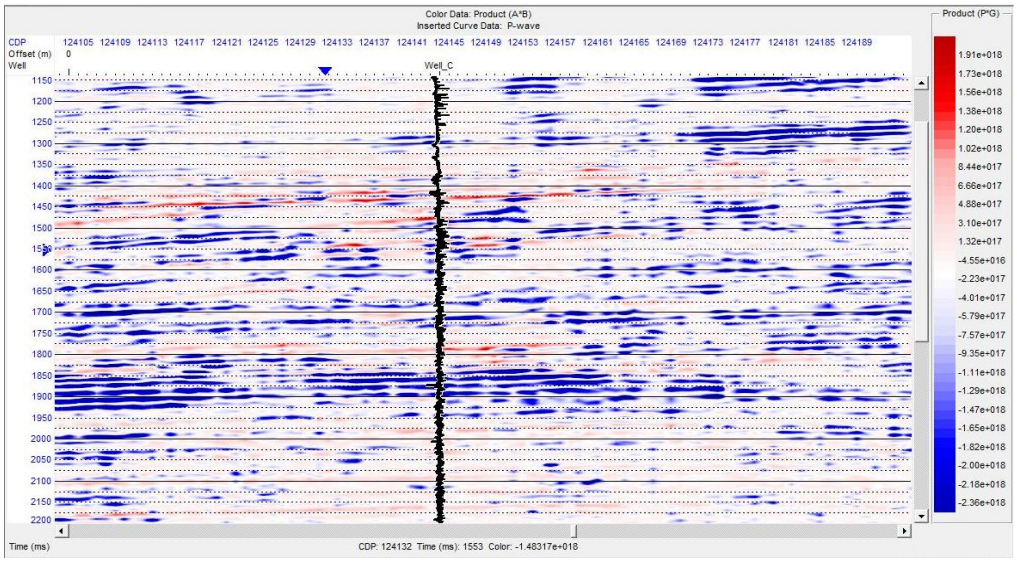

Figure 4.8 AVO attribute volume color data product (A*B).

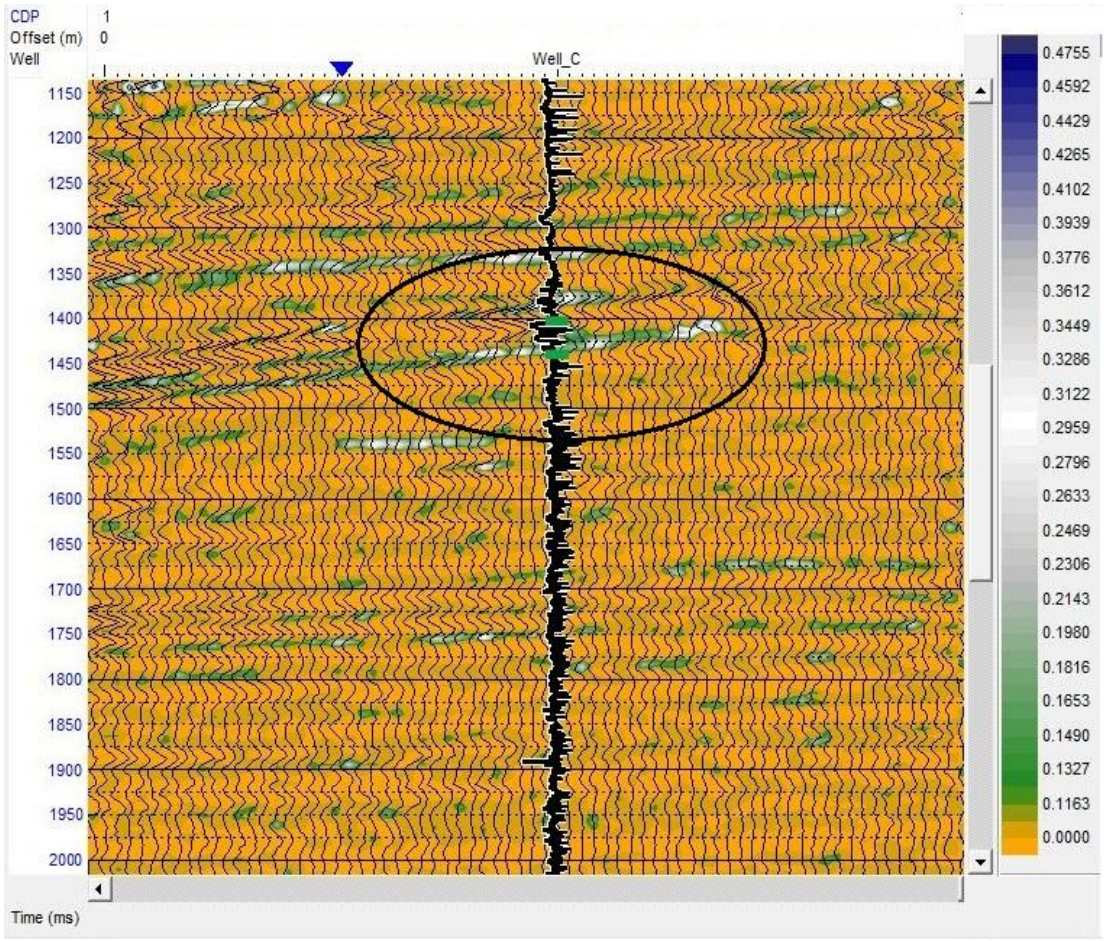

Figure 4.9 AVO attribute volume color data scaled Poisson's Ratio.

8. Crossplotted the intercept versus the gradient. The Class 3 type was observed. We filtered zones with different colors; general trends are shown in grey, top of the reservoir is in yellow, and the base of the reservoir is shown in green. These zones plotted on the CDP stack as colored and the top and the base of the reservoir marked clearly (Figure 4.10).

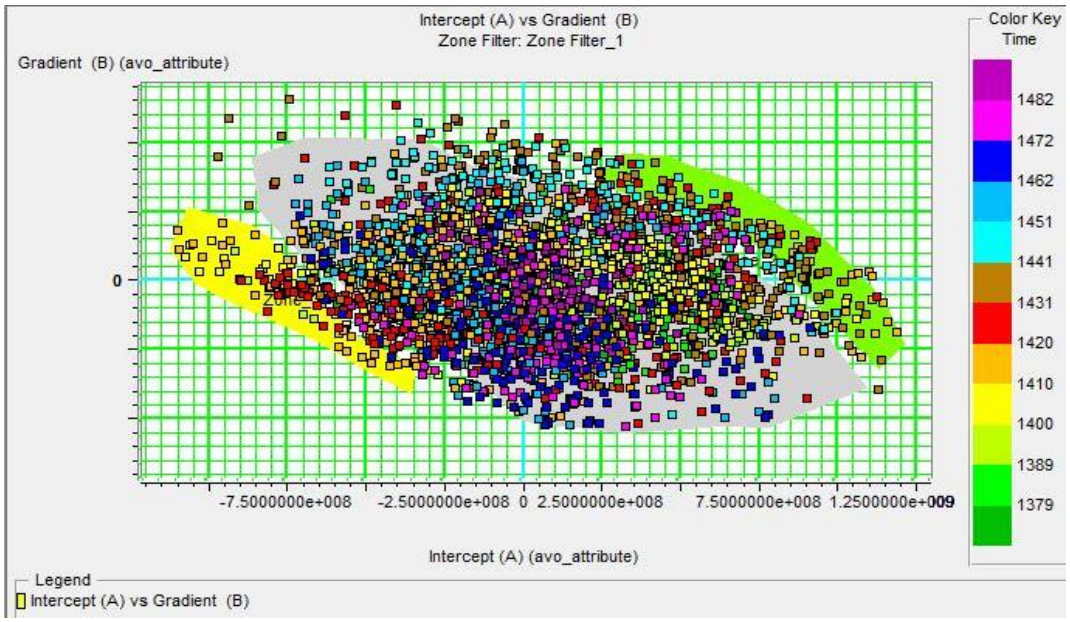

Figure 4.10 Crossplot intercept vs gradient.

9. Performed AVO curve analysis on the synthetic data and concluded that it is Class 4 on the crossplot; however, it was previously interpreted as Class 3.

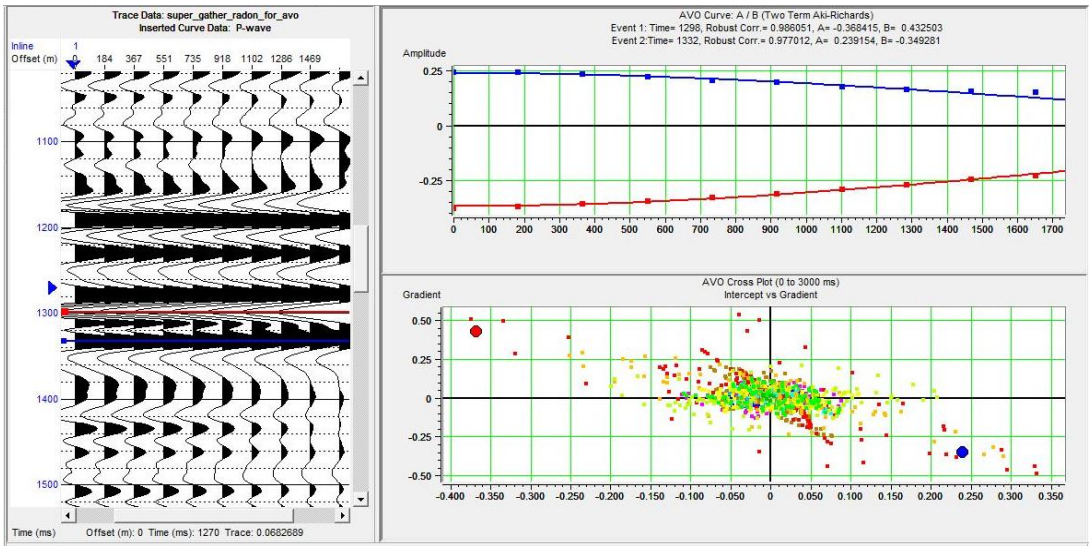

Figure 4.11 AVO response from the Aki-Richard's synthetic gather.

4.3.3 AVO Inversion Application

We performed three inversion methods for the data to enhance the vertical resolution and to compare the results. The Hampson-Russell Strata tool was used for the inversion processes.

4.3.3.1 The Simultaneous Pre-stack Inversion and The Lambda-Mu-Rho Inversion

In this section, we performed a model-based Simultaneous Inversion to obtain impedances for P- and S-wave (Zp and Zs) and density (ρ).

We followed the below steps to perform the simultaneous inversion process on the Strata section:

1. Loaded the previously created angle gather and three previously picked horizons as inputs.
2. Extracted two wavelets; a 9 degree near angle wavelet and a 27 degree far angle wavelet (Figure 4.11).

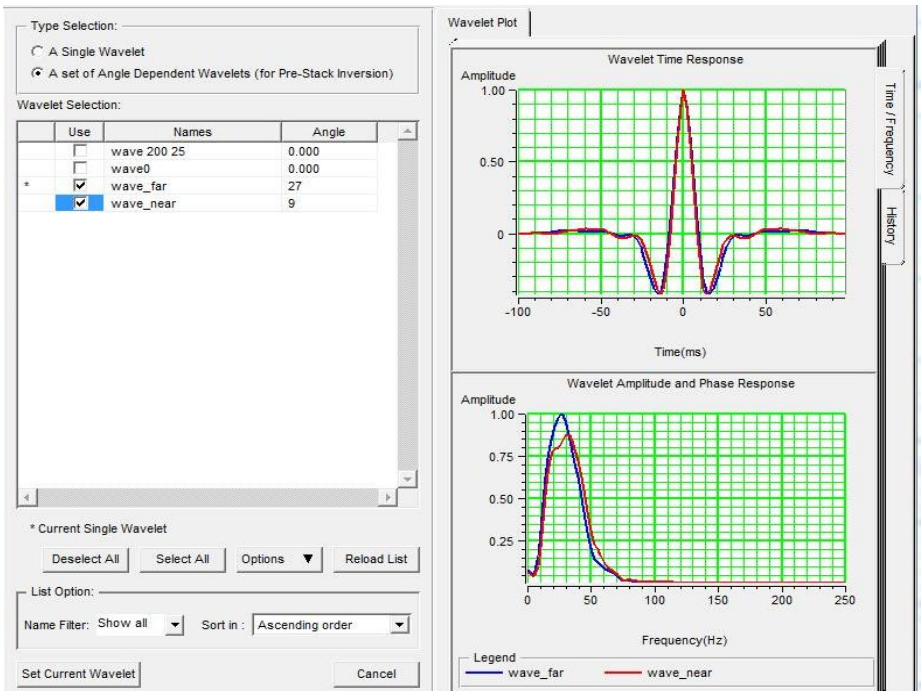

Figure 4.12 Near and far extracted wavelet in time and frequency domain.

3. Selected initial model values for Zp, Zs, and ρ from the well logs.

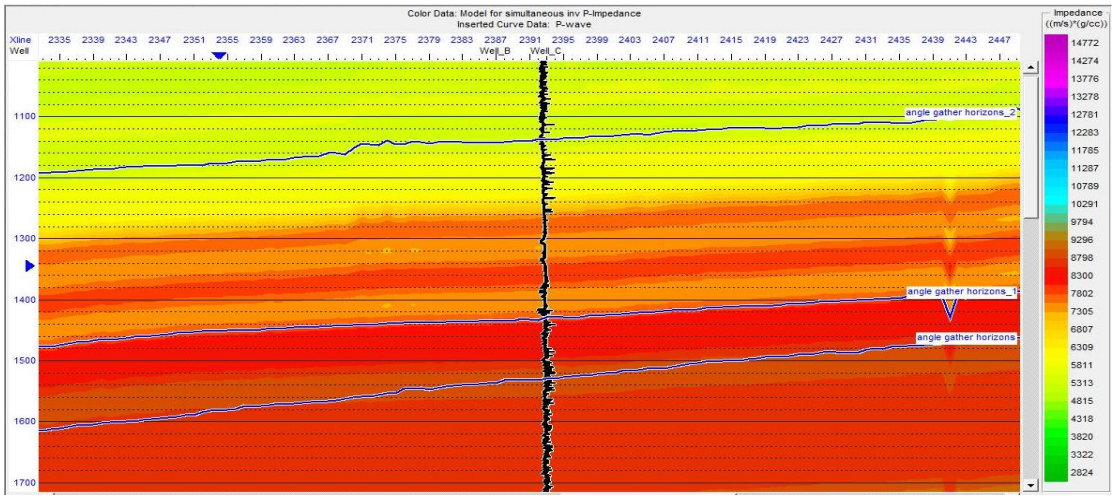

Figure 4.13 Model input for inversion with 3 picked horizons display color data P-impedance.

4. Calculated optimal values for the k and m using the actual input logs.

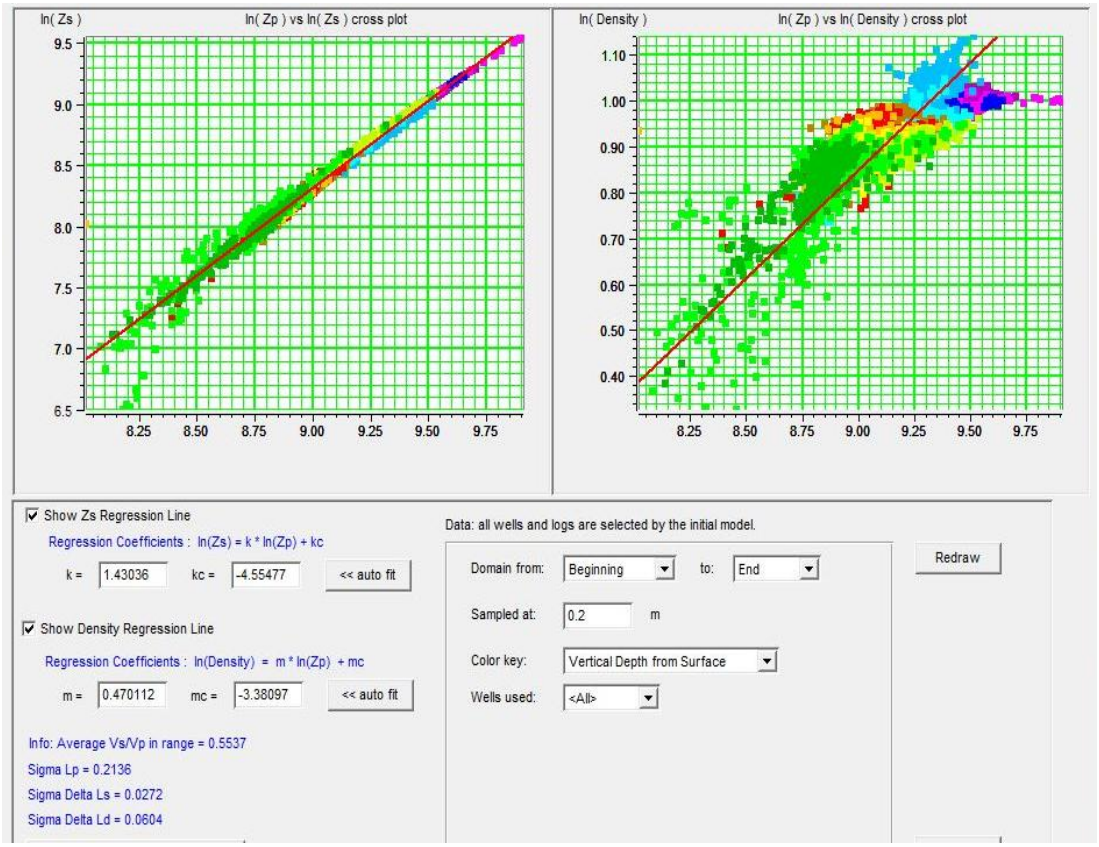

Figure 4.14 Regression line fitting and calculation of regression coefficient (k, kc, m, and mc).

5. Calculated the final values of Zp, Zs, and ρ.

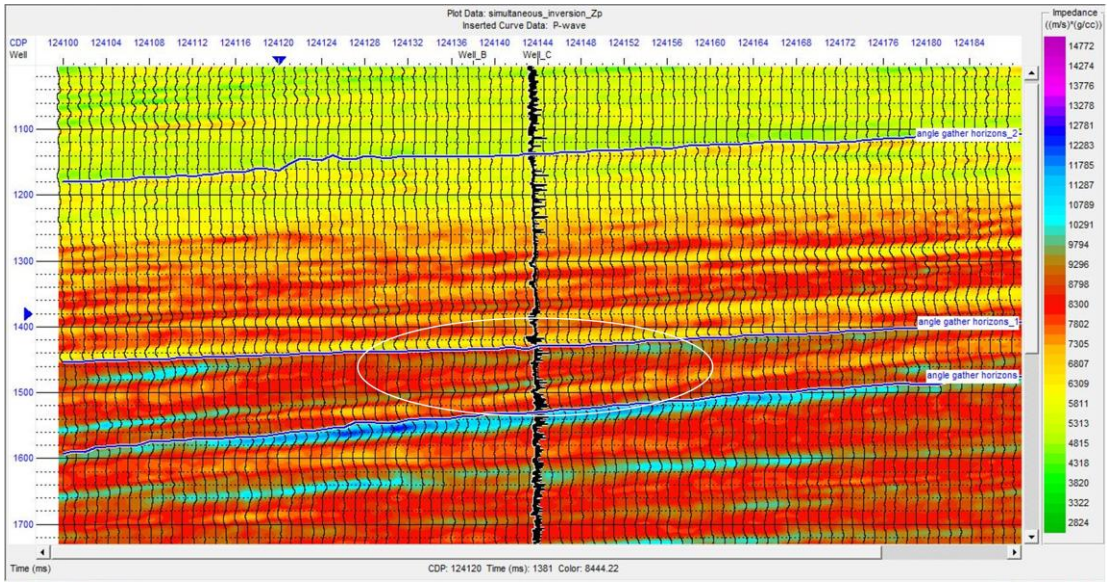

Figure 4.15 Simultaneous inversion result color data P-wave impedance (Zp).

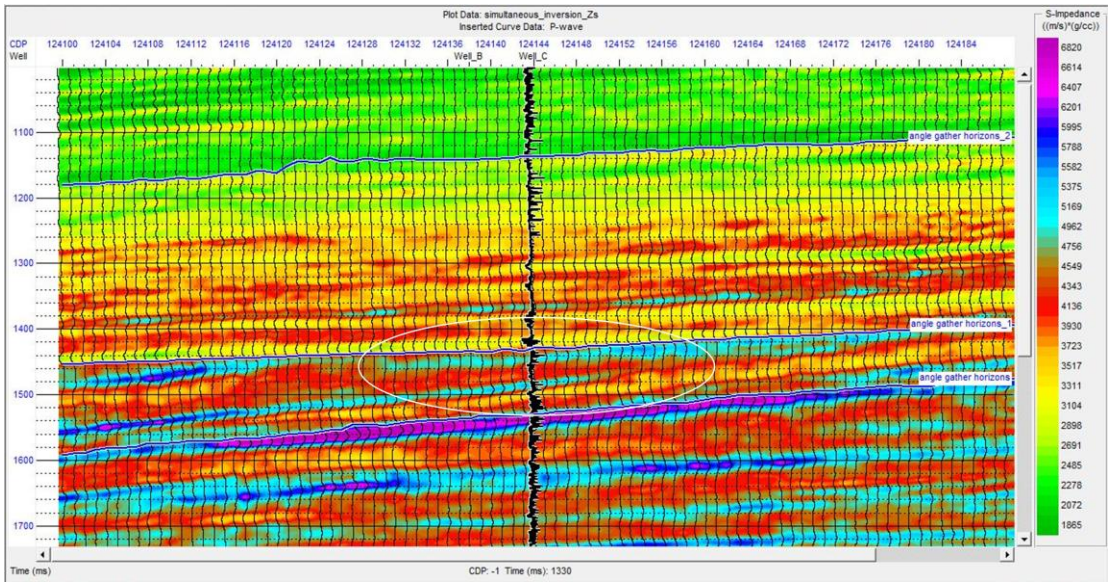

Figure 4.16 Simultaneous inversion result color data S-wave impedance (Zs).

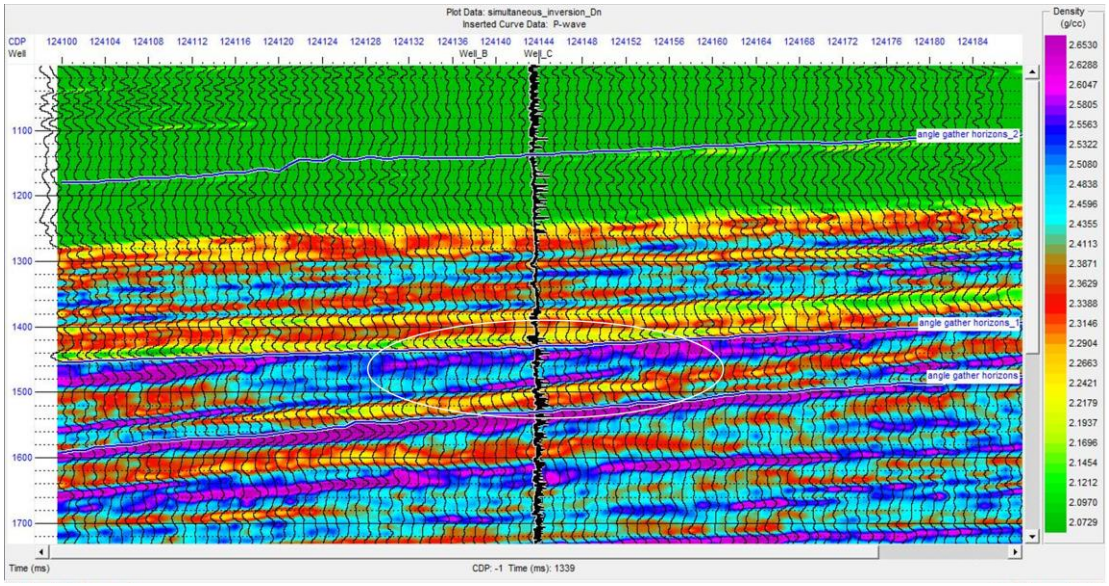

Figure 4.17 Simultaneous inversion result color data density (ρ).

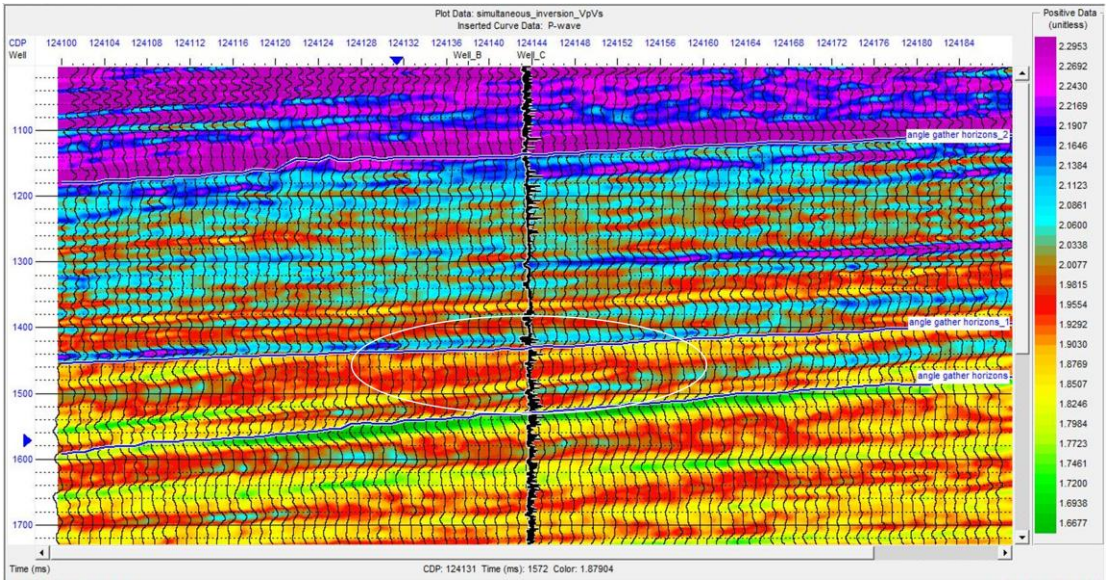

Figure 4.18 Simultaneous inversion result color Vp/Vs.

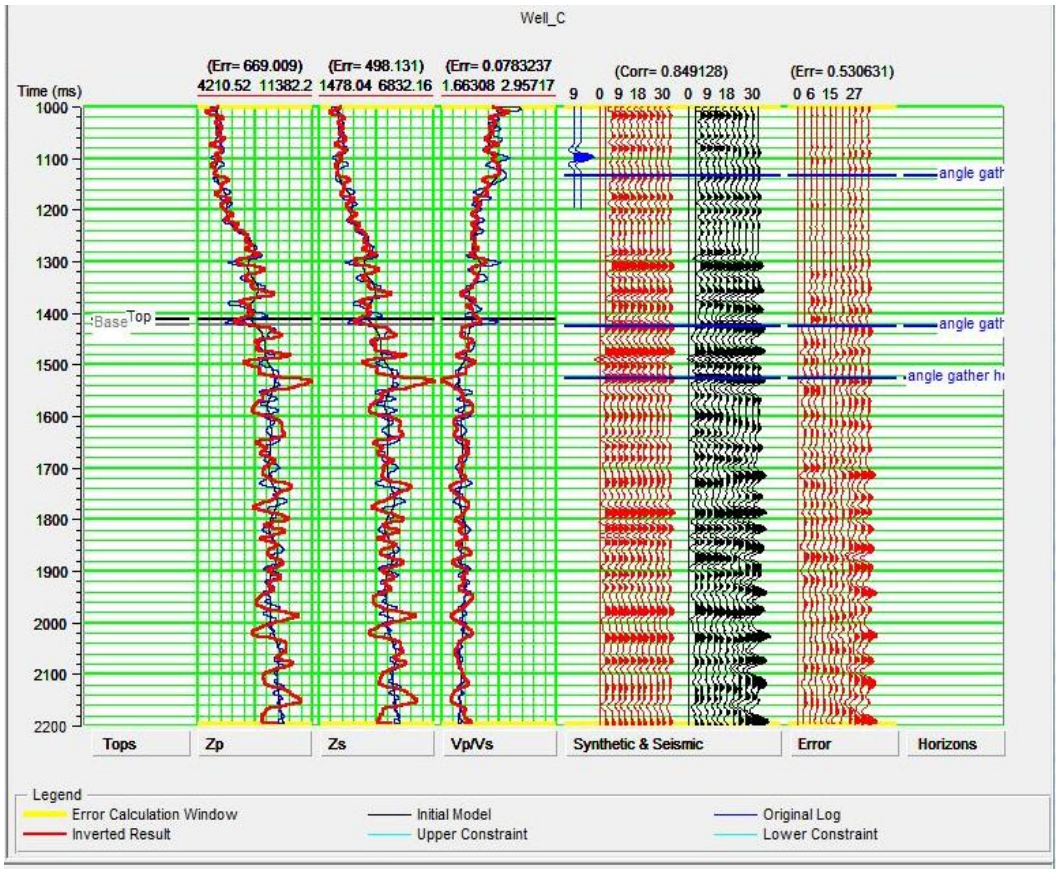

Figure 4.19 Comparison between real data and calculated data.

In this case, the initial model is shown in blue lines and the inverted result is shown in red lines.

Ones we have estimated the Zp and Zs parameters from the Simultaneous Inversion, we performed the Lambda-Mu-Rho Inversion. The obtained parameters were used in the inversion to produce our Lambda-Rho and the Mu-Rho volumes. This inversion is very beneficial to remove the effect of density from the seismic data. In this section, we simply took the estimates from the inversion and transfer them into the Lambda-Rho and Mu-Rho volumes using the Hampson-Russell software's Strata tool.

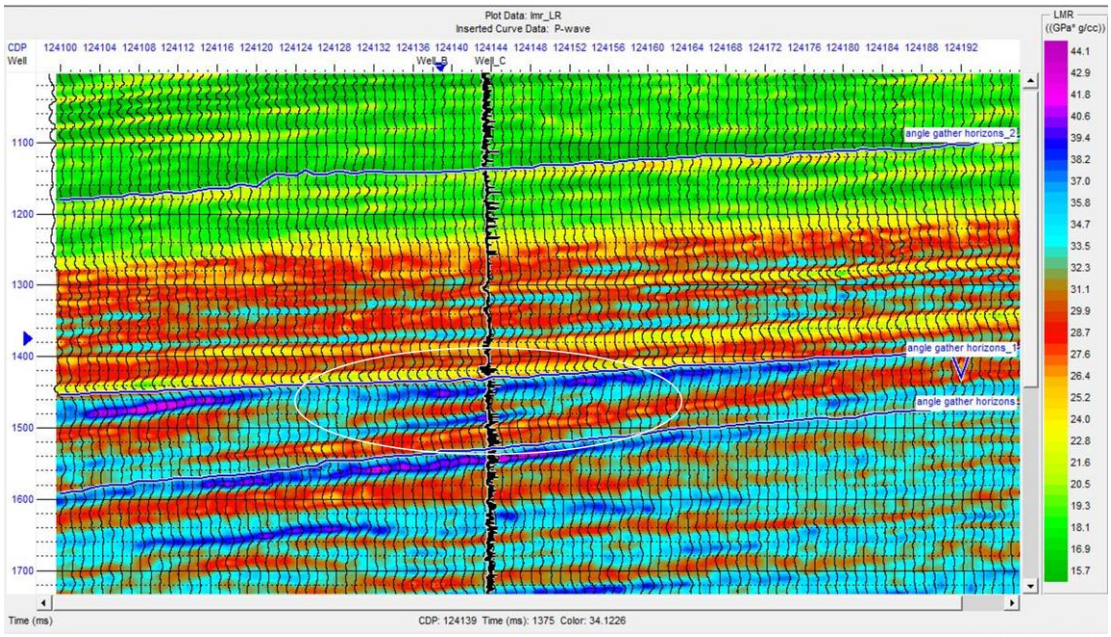

Figure 4.20 LMR inversion result LR volumes.

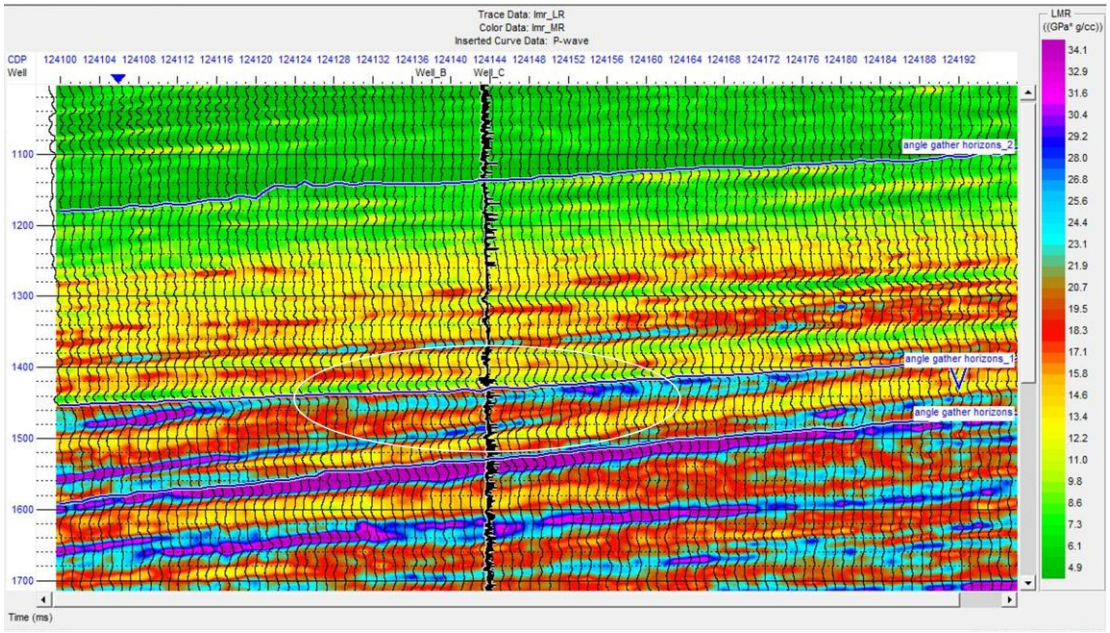

Figure 4.21 LMR inversion result MR volumes.

4.3.3.2 Elastic Impedance Inversion

The Elastic Impedance Inversion is a post-stack inversion technique performed using both the AVO and the Strata tools in the Hampson-Russell software.

We followed these steps to perform the Elastic Impedance Inversion process using the AVO tool:

1. Calculated near and far elastic impedance values with well logs using the Transform tool.
2. Created two range-limited stacks from the super gather volume using a 9 degree near angle and a 27 degree far angle.

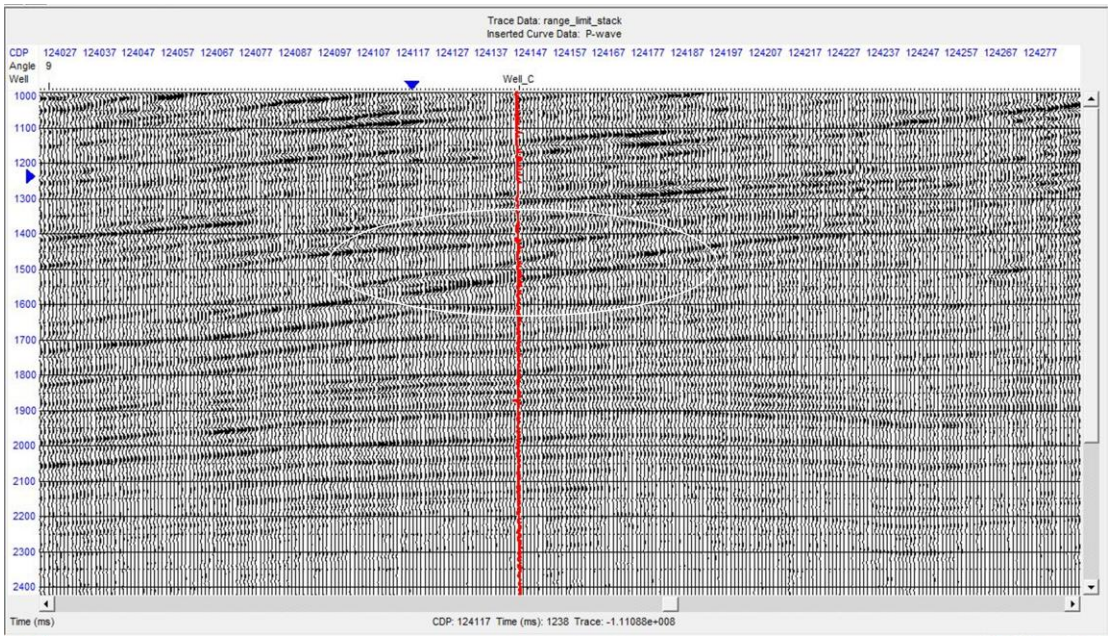

Figure 4.22 Range-limited near angle (9 degree) stack.

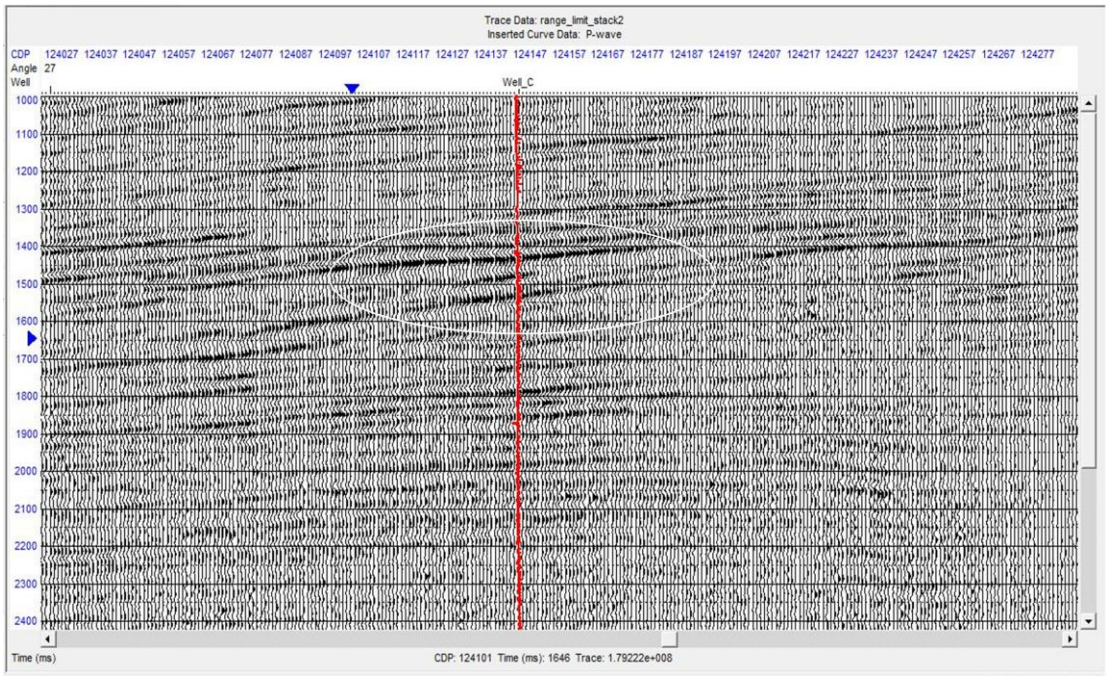

Figure 4.23 Range limited far angle (27 degree) stack.

3. Inverted values using the Strata tool.

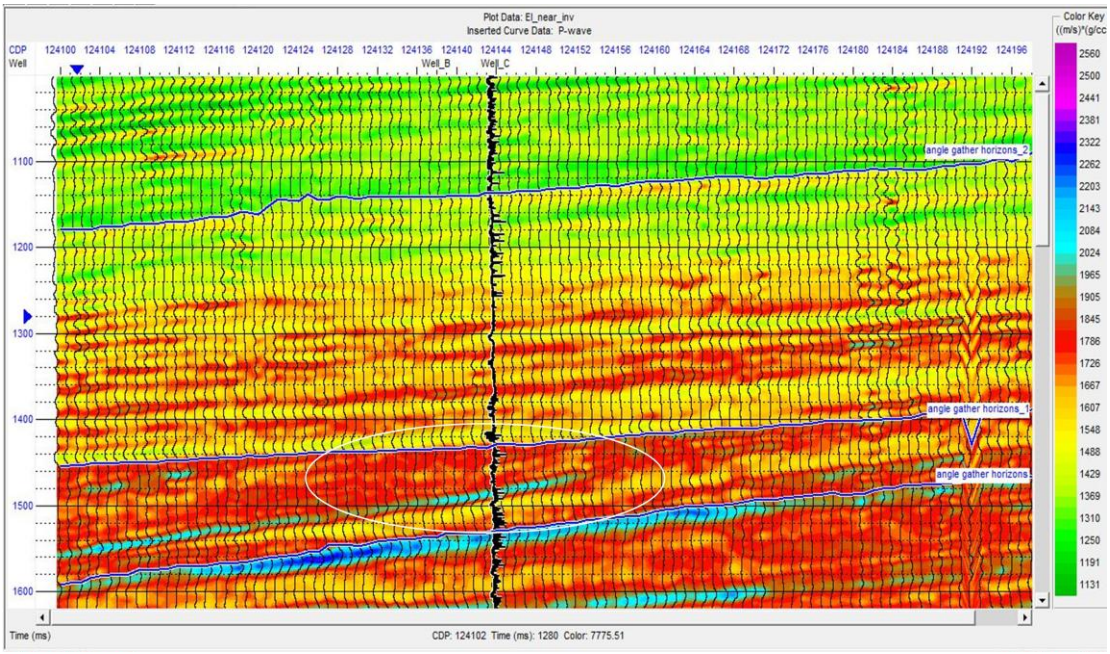

Figure 4.24 Elastic Impedance Inversion result for near degrees.

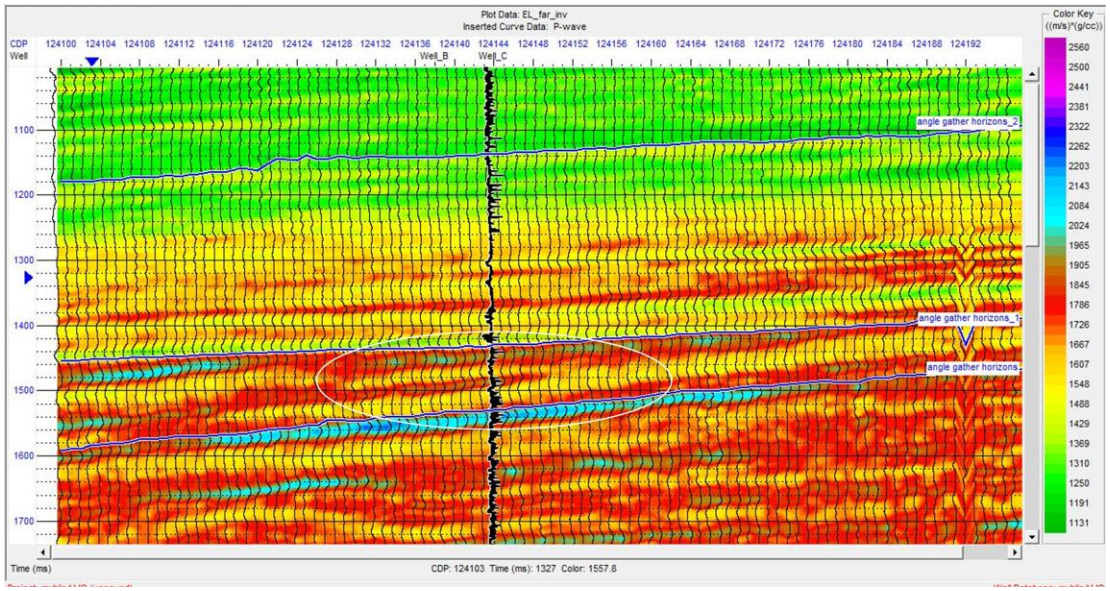

Figure 4.25 Elastic Impedance Inversion result for far degrees.

4. Calculated the elastic impedance values as outputs of the inversion process. We crossplotted those values to identify the zone of interest.
5. Filtered zones with different colors; general trends are shown in grey, and the top of the reservoir is shown in red.

Chapter 5: Results

In this chapter, we will discuss all the results obtained from the different stages of our investigations. We will show the crossplot displays which were filtered and colored zones from all processes.

Conventional AVO analysis and inversion results will be discussed in this section.

5.1 Conventional AVO Analysis Result

The zone of interest was determined between 1400 and 1426 ms depending on low GR, Vp, Vs, and RHOB log values. After stretching and shifting data 76ms we achieved a 0.94 correlation coefficient in the seismic-well tie menu. We used super gathers to determine the incident angle after the successful seismic-well tie process. We decided the zone of interest's maximum angle of incidence is 36 degrees.

We calculated intercept and gradient values, and crossplotted them using the AVO tool. We observed the AVO type Class 3.

Moreover, we performed extensional AVO curve analysis to satisfy the current class with the Aki-Richard's synthetic gather. We observed the Class 4 type. We concluded that a very large value of intercept A and a small change in Poisson's Ratio caused a reversal which is termed a Class 4 anomally (Castagna *et al.*, 1995).

We filtered zones with different colors; general trends are shown in grey, top of the reservoir is shown in yellow, and the base of the reservoir is shown in green. These zones plotted on the CDP stack as colored. The top and the base of the reservoir

marked clearly; therefore, we could be able to display the reservoir zone visibly.

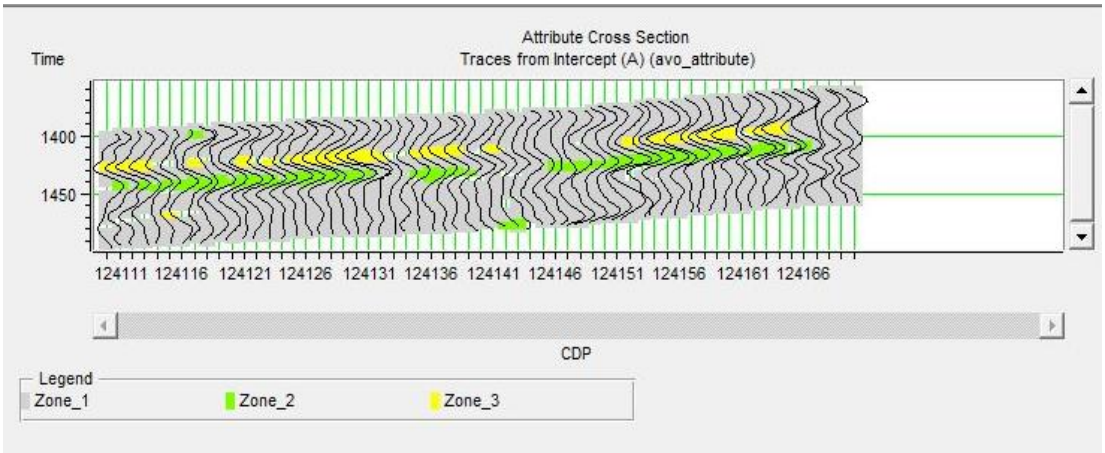

Figure 5.1 Filtered reservoir zone cross section.

In Figure 5.1, we observed that the top of the reservoir is starting at 1400ms in yellow color filtered, and the base of the reservoir is around 1445 ms in green color filtered.

We also made a crossplot calculated P-impedance from logs versus depth to observe the impedance change in the reservoir zone (Figure 5.2).

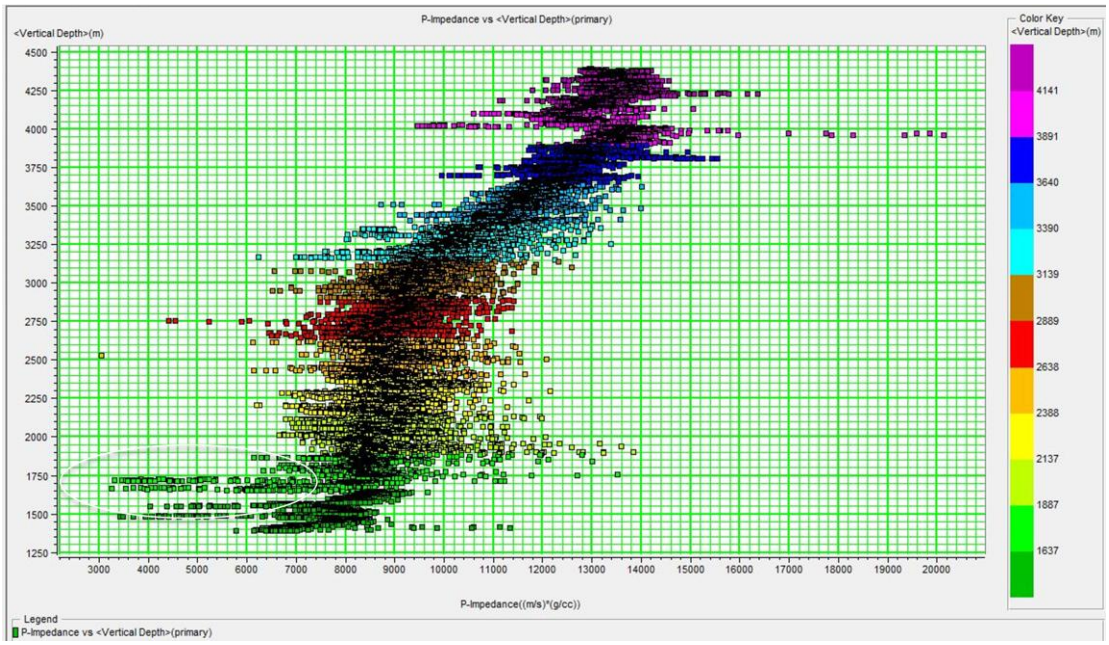

Figure 5.2 P-impedance vs depth.

In the crossplot (Figure 5.2), we observed that the lowest lined impedance values at 1700-1750 meters corresponding at 1400 ms in time which is our reservoir zone.

Another crossplot made between P-reflectivity and the depth was to observe the reflections at the top and the base of the reservoir (Figure 5.3).

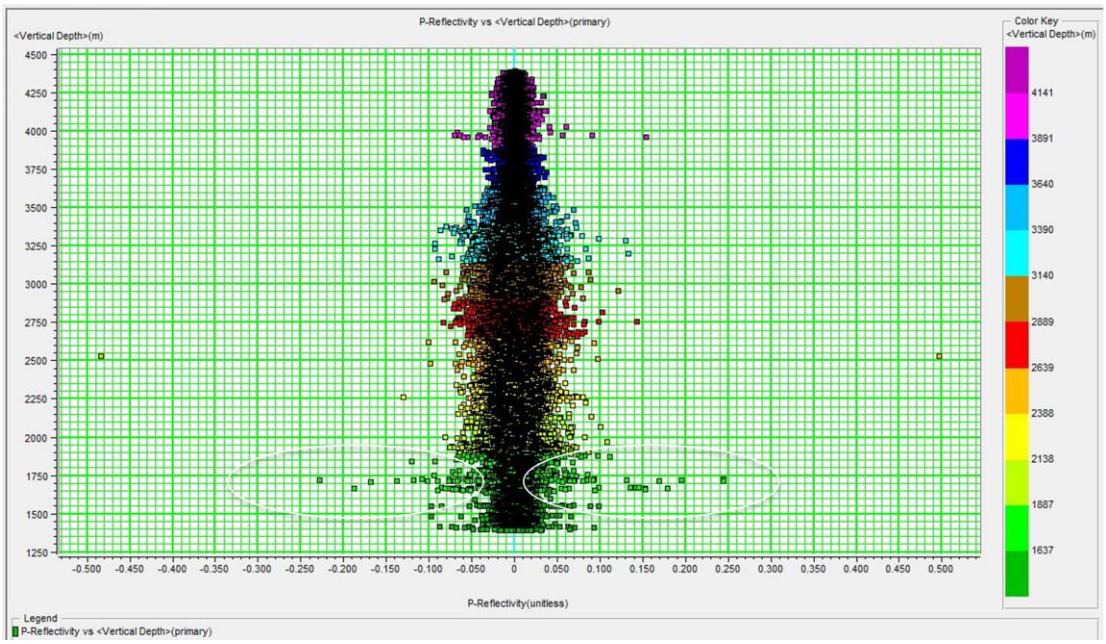

Figure 5.3 P-reflectivity vs depth.

We observed a very robust linear trend between -0.05 and 0.05 reflectivity values. We also observed strong negative and positive P-reflectivity values at the reservoir zone that produce the bright spot (Figure 5.3).

5.2 AVO Inversion Analysis Results

We could not display reservoir zone in the AVO volume attribute sections; therefore, we performed three different inversion methods to increase the vertical resolution.

In the first inversion method, we performed the Simultaneous Pre-stack Inversion and obtained P- and S-wave acoustic impedances (Zp and Zs) and density (ρ). The inversion results were crossplotted and filtered with different colors for the Vp/Vs ratio and the S-wave acoustic impedance (Zs); general trends are in grey, and the

reservoir zone is shown in red (Figure 5.4 and 5.5).

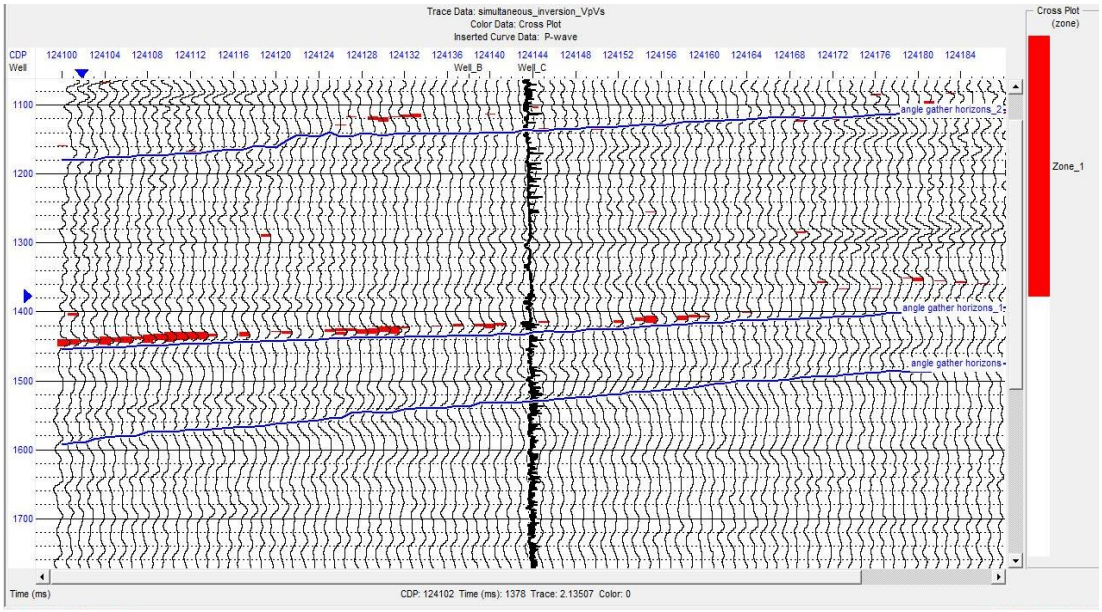

Figure 5.4 Filtered crossplot display for inverted Vp/Vs.

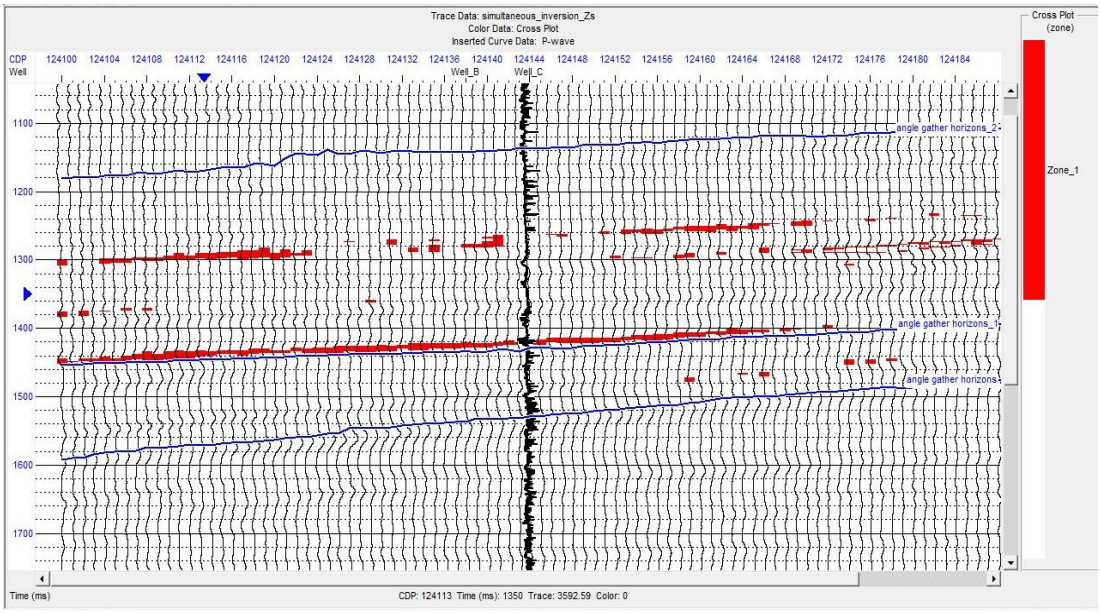

Figure 5.5 Filtered crossplot display for inverted Zs.

We displayed the zone clearly at 1400 ms in the S-wave acoustic impedance crossplot; though, we could not obtain a strong reservoir signature in the Vp/Vs and Vp crossplots.

In the second inversion method, we performed the LMR Inversion and obtained LR and MR values using the previously calculated Zp and Zs values. The LR and MR inversion results crossplotted and filtered with different colors; general trends are shown in grey, and the reservoir zone is shown in red.

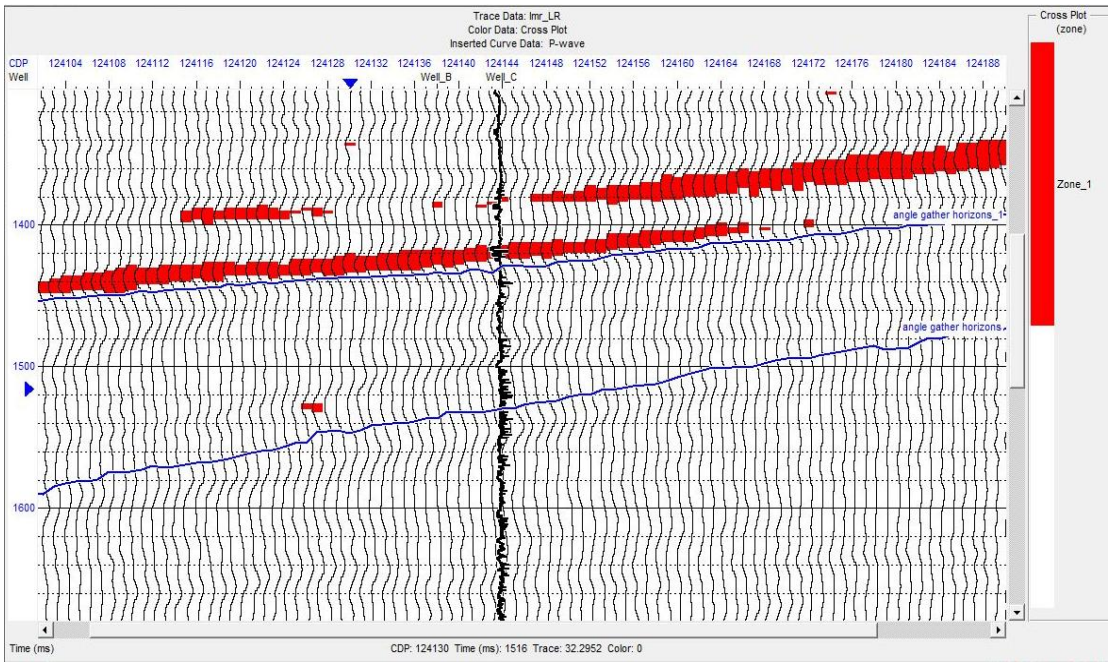

Figure 5.6 Filtered crossplot display for LR and MR from the LMR Inversion.

We marked the reservoir zone at 1400ms successfully; yet, we still have captured another zone around1350 ms (figure 5.6). We believe that this inaccuracy could be an inversion error caused by inaccurate parameters or noise effects.

The last inversion method we performed is the Elastic Impedance Inversion technique. We created range-limited stacks as inversion inputs (Figure 5.7).

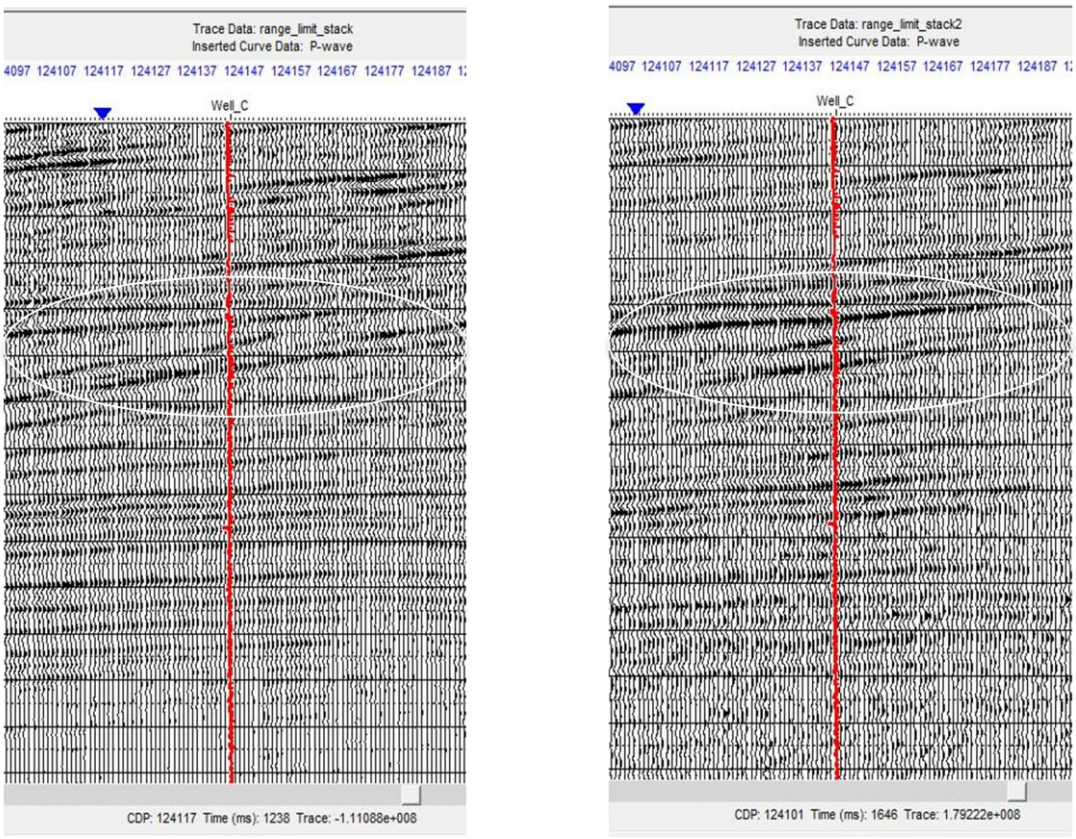

Figure 5.7 The near angle (left) and far angle (right) stacks.

Here are the near angle (9°-18°) and far angle (18°-27°) stacks from the data. We noticed that the "bright-spot' event at about 1400ms is stronger on the far-angle stack, than it is on the near-angle stack. This is a common signature of a gas-sand-induced bright spot.

After performing the Elastic Impedance Inversion, we traditionally crossplotted the results and filtered with different colors; general trends are presented in grey, the

reservoir zone is displayed in red.

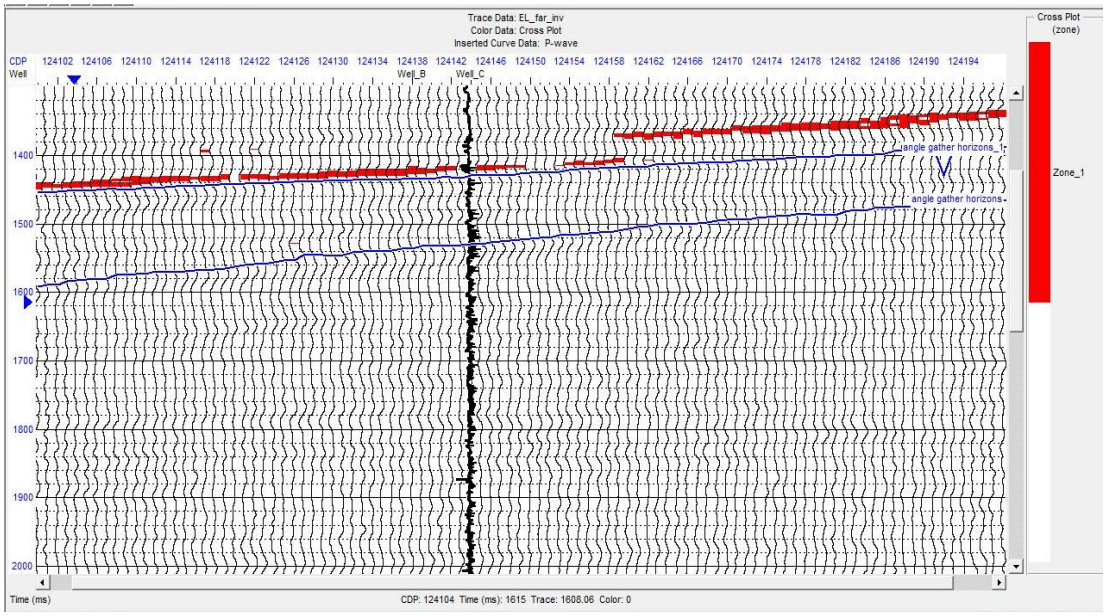

Figure 5.8 Filtered crossplot display from elastic impedance inversion results.

As we observed in the range-limited stacks, we noticed that the "bright-spot' event, at about 1400ms, is stronger on the far-angle inverted stack than it is on the near-angle inverted stack.

Conclusion:

Despite various assumptions and limitations associated with the different models and approaches employed within the context of this thesis study, the following conclusions can be made:

- Well log interpretations and the crossplots from the logs helped us to have valuable information about the reservoir location.

- We followed the conventional analysis methods to investigate the gas reservoir at 1700m. The reservoir characteristic could not be observed in the conventional AVO analysis due to the reasons; the reservoir thickness was below the tuning thickness and the noisy data.

- Applying the Radon Noise Suppression and the Trim Statics steps increased the data quality, but they could not help to observe the reservoir characteristic in the conventional data.

- The Class 3 AVO was determined from the crossplotted intercept and the gradient values. We performed an extensional AVO curve analysis to satisfy the current class with the Aki-Richard's synthetic gathers and then we observed the class 4. We concluded that a very large value of intercept A and a small change in Poisson's Ratio caused a reversal which is termed a Class 4 anomaly (Castagna *et al*., 1995).

- We performed three different inversion methods to enhance the vertical resolution; consequently, we were able to image the reservoir signature at 1400 ms from the inversion results.

- In the Elastic Impedance Inversion results, we clearly observed that the "bright-spot" event at about 1400 ms which is stronger on the far-angle stack than it is on the near-angle stack.

At the end of our project, we can conclude that the AVO inversion analysis methods can help the seismic interpreter to better understand physical properties of the interest zone and the structural features of the area; however, the conventional AVO inversion analysis fails to identify the reservoir. Furthermore, the inversion techniques can help to map the reservoir zone in a better way by increasing the vertical resolution. Additionally, noise suppression methods by preserving amplitude are very crucial to obtain valuable results. The best way to be certain about the results is to validate them with synthetics.

References:

Castagna, J. P., and Smith, S. W., 1995, Comparison of AVO indicators: a modeling study: Geophysics, Vol. 59, p. 1849-1855.

Castagna, J. P., Swan, H. S., Foster, D. L., and Peddy, C. A., 1998, Framework for AVO gradient and intercept interpretation: Geophysics, Vol 63, p. 948-956.

Cooke O.A., and Schneider, W.A., 1983, Generalized linear inversion of reflection seismic data, Geophysics, Vol. 48, p. 665-676.

Huvaz O., Sarıkaya H., and Nohut O. M., 2005, Nature of a regional dogleg pattern in maturity profiles of the Thrace Basin, northwestern Turkey: A newly discovered unconformity or a thermal anomaly?: AAPG Bulletin, Vol. 89, No. 10, p. 1373-1396.

Lamb, W. J., Zhu, X., McMechan, G. A., Greenberg, M., and Castagna, J. P., 1992, Elastic wave propagation in composite media: Geophysics, Vol. 57, p. 1155-1165.

Liu L., Cao S., and Wang L., 2011, Poroelastic analysis of frequency-dependent amplitude-versus-offset variations. Geophysics, Vol. 76, No. 3, p. 31-40.

Mahob, P.N. and Castagna, J. P., 2003, AVO polarization and hodograms: AVO strength and polarization product: Geophysics, Vol. 68, p. 849-862.

Ren H., Goloshubin G., and Hilterman, F.J., 2009, Poroelastic analysis of amplitude-versus-frequency variations: Geophysics, Vol. 74, No. 6, p. 41-48.

Russell, B.H., 1991, "Introduction to seismic inversion methods", SEG continuing Education Short Course.

Rutherford, S.R., and Williams, R.H., 1989, Amplitude-versus-offset variations in gas-sands: Geophysics, Vol. 54, p. 680-688.

Sarkar D., Castagna J.P., and Lamb W.J., 2001, AVO and velocity analysis: Geophysics, Vol. 66, No. 4, p. 1284-1293.

Tiwary D.K., Bayuk I. O., Vikhorev A.A., and Chesnokov E.M., 2007, Comparison of seismic upscaling methods: From sonic to seismic. Geophysics, Vol. 74, No. 2, p. 3-14.

Turgut, S., Turkaslan M., and Perincek, D., 1991, Evolution of the Thrace

sedimentary basin and its hydrocarbon Eocene sediments prospectivity. In: Generation, Accumulation, and Production of Europe's Hydrocarbons (Ed. A.M. Spencer), Spec. Publ. Eur. Assoc. Petrol. Geoscientists, Vol. 1, p. 415–437.

Appendix A:

The seismic data in the ED50 Coordinate system were processed through the Kirchhoff Pre-stack Time Migration. The necessary steps were applied by Turkish Petroleum Corporation to the dataset as follows;

- Field Static Correction: Reference datum elevation 100m.
- Surface Consistent True Amplitude Correction: Shots and receivers.
- Gain Correction: T^2.
- Predictive Deconvolution: 24 μsec gap, 200 μsec filter length.
- CDP Binning: 25m x 25m.
- Wavelet Processing: 8-60 Hz Butterworth.
- Velocity analysis.
- NMO.
- Surface consistent residual statics.
- Pre-stack Kirchhoff Time Migration.